Supplementary Materials for

Reprogramming of Intestinal Glucose Metabolism and Glycemic Control in Rats After Gastric Bypass

Nima Saeidi, Luca Meoli, Eirini Nestoridi, Nitin K. Gupta, Stephanie Kvas, John Kucharczyk, Ali A. Bonab, Alan J. Fischman, Martin L. Yarmush, Nicholas Stylopoulos*

*Corresponding author. E-mail: Nicholas.Stylopoulos@childrens.harvard.edu

Published 26 July 2013, Science 341, 406 (2013)

DOI: 10.1126/science.1235103

Materials and Methods

Animals: The animal experiments and animal care were performed in compliance with and were approved by the Institutional Animal Care and Use Committees of Boston Children's Hospital and Massachusetts General Hospital, Boston, MA. Male rats (Long Evans and Goto-Kakizaki) were used for all studies. In diet-induced obese (DIO) Long Evans rats, obesity was induced by feeding the animals *ad libitum* with a high-fat diet (HFD), which provides 60% of total energy as fat, 20% as carbohydrate, and 20% as protein (D12492 diet, Research Diets Inc., New Brunswick, NJ). At the time of surgery, DIO rats weighed 675 ± 25 g. Animals were individually housed and were maintained on 12-h light, 12-h dark cycle (lights on at 0700 h) in facilities with an ambient temperature of 19–22 °C and 40–60% humidity.

Surgery and post-surgery procedures: Animals were fasted overnight. During the surgical procedures, they were maintained on inhalation anesthesia (isoflurane 1–4%). Rats were kept without food for 24 h after the surgery. After evaluating the health and behavior of each animal, a liquid diet was reintroduced 48–72 h following the operation. Beginning on postoperative day 7, the rats were switched to their preoperative diet.

Roux-en-Y gastric bypass (RYGB): The total length of the small intestine was measured, the ligament of Treitz was identified, and the jejunum was divided at the appropriate distance downstream of this ligament. An end-to-side jejuno-jejunostomy and a gastro-jejunostomy were created with a 7-0 silk or prolene running suture. A pouch was created by transecting the stomach. The gastric artery was preserved and only the small vascular branches were cauterized. The laparotomy was closed with a 5-0 polydioxanone (PDS) suture in two layers.

Esophago-stomach jejunal loop interposition (ES-JLI) model: A loop of jejunum was isolated and transposed between the esophagus and the stomach. After the procedure, nutrients flow from the esophagus through the esophago-jejunostomy to the transposed jejunal loop and then through the jejuno-gastrostomy to the stomach, the duodenum, the jejunum, and the rest of the gastrointestinal tract. The anastomoses were performed with 7-0 silk running sutures.

Sham operation: In all experiments, rats undergoing a sham operation were used as controls. The sham operation consisted of laparotomy, jejunal transection, and repair; and was performed in rats that were age- and weight- matched preoperatively to rats undergoing RYGB or ES-JLI.

Positron emission tomography-computed tomography (PET/CT): Rats were fasted overnight. They were imaged with a microPET Focus 220 (Siemens Medical Solutions USA, Inc., Malvern, PA) coupled with a portable CereTom CT scanner (NeuroLogica Inc., Danvers, MA) 50 min after a tail vein injection of approximately 2 mCi of 2-deoxy-2-(18F)fluoro-D-glucose ([18F]FDG). Each rat was anesthetized with isoflurane, positioned in a rat head holder in the PET camera gantry, and imaged for 5 min per bed position, for a total of 5-6 bed positions. After the PET imaging, a whole-body CT of the rat was acquired. The list mode data was Fourier re-binned to a single frame and reconstructed, using the map technique at zoom 2. The CT data were used for attenuation correction. Dead time and random corrections were used for each bed position. Finally, data from all the bed positions were assembled to a whole-body format using ASCII pro software (Siemens Medical Solutions USA, Inc., Malvern, PA).

Biodistribution analysis: Rats were fasted overnight. Each rat was administered approximately 300 µCi of [18F]FDG through the tail vein. Immediately after injection of [18F]FDG, a designated standard solution of [18F]FDG was prepared to account for natural decay of the isotope. One hr after injection, the rats were euthanized in a chamber with CO_2. Immediately, blood and tissues were collected and placed in pre-weighed glass vials. The radioactivity of the samples was measured in a γ-counter and the weight of each vial was measured again (to calculate the wet weight of each organ). [18F]FDG tissue uptake levels were expressed as a percentage of injected dose per gram of tissue. [18F]FDG blood levels were expressed as a percentage of injected dose per ml of blood.

Oral glucose tolerance test: Rats were fasted overnight. The following morning, rats were weighed and a glucose solution (1 g glucose/kg body weight) was administered orally. Blood glucose levels were measured before glucose administration (time 0) and 10, 20, 30, 45, 60, and 120 min after oral glucose administration. Blood glucose levels were measured using a blood glucose meter (LifeScan Inc., Milpitas, CA) by cutting the tail of each rat and gently massaging 35-50 µl of blood onto a glucose test strip.

Insulin tolerance test: Animals were fasted for 5 hr (from 7 am to 12 pm) and received an intraperitoneal injection of insulin (0.75 IU/kg body weight). Blood glucose levels were measured at 10, 20, 30, 45, 60, and 120 min, as described under the oral glucose tolerance test.

STZ-induced diabetes: To induce diabetes, Long Evans rats, maintained on normal chow, were intraperitoneally injected with 60 mg/kg or 100 mg/kg of streptozotocin (STZ, Sigma Aldrich Co LLC, St Louis, MO) dissolved in citrate buffer (0.1 M sodium citrate, pH 4.5).

Histology and Immunohistochemistry (IHC): Rats were euthanized in a chamber with CO_2. Tissues were immediately collected, snap frozen in liquid nitrogen, and stored at -80 °C. For histology, tissues were flushed with formalin, placed into 50 ml falcon tubes of formalin, and kept at room temperature for 2 days. They were transferred to 70% ethanol and kept at 4 °C before being sent to the Animal Histology Core (Tufts Medical Center, Boston, MA) for tissue embedding in paraffin-wax and sectioning. Morphological analysis of the intestine was performed using ImageJ software (Research Services Branch, National Institutes of Health, Bethesda, MD) by analyzing 2 cm of tissue. For IHC, histology slides containing sections from the intestine were incubated for 10 min at 60 °C, and deparaffinization, rehydration, and antigen retrieval were performed with TrilogyTM pretreatment solution (Cell Marque, Rocklin, CA) in a pressure cooker (Cuisinart, East Windsor, NJ) for 10 min. Slides were allowed to cool down to room temperature and washed for 5 min twice in distilled water and once in TBS-T (Tris-EDTA, pH 7.6, 0.1% Tween20). After incubation in peroxide block for 30 min (Thermo Scientific, Billerica, MA), they were incubated for 1 h at room temperature in TBS-T with 5% goat serum, followed by an overnight incubation at 4 °C with the primary antibody. Primary antibodies were diluted as follows: GLUT-1 (Cell Signaling Technology Inc., Danvers, MA): 1:2,000; HMGCR (Biovision Inc., Milpitas, CA): 1:100; LDLR (Biovision Inc., Milpitas, CA): 1:1,000; Ki67 (Abcam, Cambridge, MA): 1:500. Slides were washed for 5 min thrice in TBS-T, followed by 30 min incubation at room temperature with biotinylated anti-rabbit secondary antibody (Thermo Scientific, Billerica, MA). Pierce ABC Staining Kit (Thermo Scientific, Billerica, MA) was used to detect the secondary antibody. Slides were stained using Dako Kit (Dako North America Inc., Carpinteria, CA), and counter-stained using hematoxylin (Thermo Scientific, Billerica, MA). Images were taken using an Olympus BX43 microscope.

Electron microscopy: Tissue was cut from the center of the Roux limb of RYGB-treated rats or corresponding jejunal segment of sham-operated rats and placed in a fixative solution (0.1 M cacodylate buffer with 2% paraformaldehyde, 2.5% glutaraldehyde, and 0.03% picric acid) provided by the Cellular Imaging Core of Boston Children's Hospital Intellectual and Developmental Disabilities Research Center (IDDRC, Boston, MA). Electron microscopy of the tissues was performed at the same core. Images were taken through a Tecnai^{TM}G^2 Spirit BioTWIN electron microscope.

Quantitative Real-time PCR: Total RNA was isolated using the RNeasy Plus Universal Tissue Mini Kit (Qiagen Inc., Germantown, MD). RNA was cleaned using the RNase-Free DNaseSet (Qiagen Inc., Germantown, MD), and 1 µg from each sample was converted to cDNA using the High Capacity RNA to cDNA kit (Applied Biosystems, Foster City, CA). Primers were designed using NCBI Primer-BLAST or were based on previously published studies. All primers were ordered from Integrated DNA Technologies Inc. (Coralville, IA). Real-time PCR was performed using the ViiA^{TM} 7 Real-Time PCR system (Applied Biosystems, Foster City, CA) under the following conditions: 10 min denaturation at 95 °C, followed by 45 cycles of 15 sec at 95 °C and 60 sec at 60 °C. Melting curves were performed for each reaction. Ct values of the gene of interest were normalized with at least four different reference (housekeeping) genes. Numerous reference genes were tested for the gene expression studies. Each of the reference genes was also initially compared against all other reference genes to determine which ones were the best. We identified 5 reference genes, that is, ribosomal protein S13 (RPS13), cyclophilin A (CYCA), ribosomal protein L22 (RPL22), ribosomal protein S16 (RPS16), β2 microglobulin (B2M), that worked consistently well.

A list of the primers used in this study is presented below. PCR reaction mixtures were loaded in triplicates into 384-well clear optical reaction plates (ABI PRISM^{TM}, Applied Biosystems, Foster City, CA) with each well containing: 1 µL of cDNA diluted 20-fold, 250 nM of each primer, Power SYBR Green MasterMix (Applied Biosystems, Foster City, CA), and nuclease-free water in 10 µL total volume.

Gene	NCBI Accession #	Sequence
GLUT-1	NM_138827	GTGCTCGGATCCCTGCAGTTCG GGGATGGACTCTCCATAGCGGTG
GLUT-2	NM_012879	TCAGCCAAGGACCCCGTCCC AAGGCCCGAGGAAGTCCGCA
GLUT-3	NM_017102	GCGCAGCCCTTCCGTTTTGC CGCTGGAGGATCTCCGTCGC

GLUT-5	NM_031741	TCGCACTGGCACTGCAGAACA GCCCCACGGCGTGTCCTATG
HK2	NM_012735	GAGTACATGGGCATGAAGGG ACTTCACAGTGAGGGTCTTC
LDHA	NM_017025	CTGATGGGAGAAAGGCTGGGAG CAGATGAGAAGTGCGTGGTCT
PKM2	NM_053297	GGGCTCCTATCATTGCTGTG CACGAAGATCAACGTCCTCA
HMGCR	NM_013134	CACCATGTCAGGGGTGCGGC AGGGACACGCAGGCTGGGAA
LDLR	NM_175762	CGTCACGCAGCCTAGAGGGGT ATCTGAGGGGCAGGCAGGCA
HMGCS1	NM_017268	CGCCAGGCCTACAGGTGGAGT TGTCCCACGAAGCCCTCGGT

MVD	NM_031062	CGTCATGGCCTCGGAAAAGCCT
		GCTTCATCCCGCTTTCCCCAGTA
CYP51A1	NM_012941	CTGCTCATCGCCTGCGCCTT
		GACTTTTCGCTCCAGCGGGCA
SREBP2	NM_001033694	AGGTCAGCCCTTGGTCCCGA
		GCGCACAGCTGCATCATCGC
PSAT1	NM_198738	TGTTTCTTTGCTTTTCGGTTAG
		CAGATTGCCCTGGTTAAACTAC
PFKFB3	NM_057135	CCAGCCTCTTGACCCTGATAAATG
		TCCACACGCGGAGGTCCTTCAGAT
G6PC	NM_013098	CTACCTTGCGGCTCACTTTC
		ATCCAAGTGCGAAACCAAAC
FBP2	NM_053716	GCTGTCCAATTCCCTGGTGA
		TCCATCCAGTGGGTCAAAGC
ABCA1	NM_178095	CCGCCTATTCTCAGATGCTC
		GGAAGGGACAAACTGTGCTG

ABCG5	NM_053754	AGCGTCAGCAACCGTGTCGG AGATGGCGTCCAGCAGCGTG
ABCG8	NM_130414	TCATGGCTGAGAAGACCAAA CTCTGACCTCCAGAGTGTTGG
CD36	NM_031561	TGCATGAATTAGTTGAACCAGGCCA CCACAGTTCCGATCGCAGCCC
RPS13	NM_130432	CACATGGTGTGGCACAGGTC GAGATCCTCAGGAAGATCAGGG
RPL22	NM_031104	GCCGCCATGGCTCCTGTGAAAA ACAGGGTGAGTGCAGTCAAGGGT
RPS16	NM_001169146	GGGGTGGCCCCAAGCTTTCC TGTGGCTGTTTTCTTGCGTCCGA
CYCA	NM_017101	GTCAACCCCACCGTGTTCTTC ATCCTTTCTCCCCAGTGCTCAG

B2M	NM_012512	CCTCAACTGCTACGTGTCTCAG CCAGTCCTTGCTGAAGGACAG
KLF15	NM_053536	AGCTGCAGACAAGTCACCAC TATCCCACTGGGCATTTCGG
PEPCK-C	NM_198780	TTTGGTCAACAACTGGGCCT TTGGTTTTCCCACAGGCACT
FBP1	NM_012558	CCATCATAATAGAGCCCGAGAAGA CTTTCTCCGAAGCCTCATTAGC

Tissue lysate preparation, SDS-PAGE, and Western blotting: Frozen intestinal tissues were crushed to powder using liquid nitrogen cooled mortar and pestles (CoorsTek, Golden, CO). Frozen powder was transferred to conical tubes and 1.5 volumes of ice cold RIPA buffer (Sigma Aldrich Co LLC, St Louis, MO) containing 1X protease inhibitors (complete EDTA-free, Roche Diagnostics, Indianapolis, IN) were added to each sample. Samples were homogenized for 40 sec on ice, using a stand homogenizer (LabGEN 700, Cole Parmer North America, Vernon Hills, IL). Samples were rotated at 4 °C for 15 min and centrifuged at 11,000 rpm for 20 min. Protein concentration of each lysate was determined using a Bradford protein assay (BioRad Laboratories, Hercules, CA). Protein lysates were heated at 60 °C (if GLUT-1 expression was to be tested) or 95 °C (for all other proteins of interest) for 5 min with Laemmli buffer and separated by sodium dodecyl sulfate polyacrylamide gel electrophoresis through 12.5% SDS or 4-20% gradient gels (PreciseTM Protein Gels, Thermo Scientific, Billerica, MA). Proteins were transferred to polyvinylidene difluoride membranes (Immobilon-P, EMD Millipore, Billerica, MA) at 400 mA for 75 min at 4 °C, using a wet transfer system (Hoefer Inc., Holliston, MA). Membranes were blocked in 5% milk dissolved in PBS-T (1X PBS + 0.1% Tween20) for 1 h at room temperature. Primary antibodies were diluted in 5% milk or 5% bovine serum albumin in PBS-T according to manufacturer's recommendations. The following antibodies from Abcam (Cambridge, MA) were used at 1:1,000 dilution: GLUT-1 and H6PD whereas GAPDH was used at 1:2,500 dilution. The following antibodies from Cell Signaling Technology (Danvers, MA) were used at 1:1,000 dilution: HK2, PDH, PDHK1, PKM2, phospho-PKM2, CDC2, cyclinD1, cyclinE, PI3K p110α, PI3K p110β, PI3K p110γ, phospho-Akt (Thr308), phospho-Akt (Ser473), phospho-c-Raf (Ser259), phospho-GSK3 (Ser9), and phospho-PDK1 (Ser241). HMGCR and LDLR antibodies from BioVision (Milpitas, CA) were both used at 1:250 dilutions. Blots were incubated with primary antibodies overnight at 4 °C. After washing with PBS-T, blots were incubated with goat anti-rabbit IgG HRP (Abcam, Cambridge, MA) or goat anti-mouse IgG HRP (Santa Cruz Biotechnology Inc., Santa Cruz, CA) in 5% milk dissolved in PBS-T for 1 h at room temperature. Membranes were developed using Pierce ECL Western Blotting Substrate (Thermo Scientific, Billerica, MA).

B2M was chosen as the most appropriate loading control after examining several other loading controls, such as β-actin and GAPDH. We found β-actin to be regulated in the intestine after RYGB, as shown in the figure below.

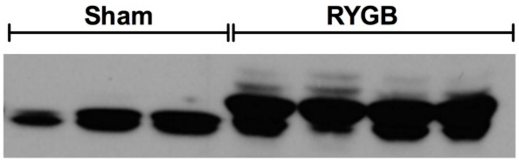

GAPDH could not be used, because it is a glycolytic enzyme and was also up-regulated in the intestine, after RYGB.

Metabolic assays and ELISA kits: The G6PD activity assay (Biovision Inc., Milpitas, CA), the GLP-1 (7-36) assay (Phoenix Pharmaceuticals Inc., Burlingame, CA), the serum insulin, GLP-2, and PYY assays (Alpco Diagnostics, Salem, NH) were performed according to manufacturer's instructions. All the samples were performed in triplicates. GLP-1 levels were measured 15 min after a meal of TwoCal (Abbott Nutrition, Columbus, OH).

Metabolomic profiling: Metabolites were extracted and analyzed according to the methods previously described *(33, 34)*. Quantitative metabolomic profiling was performed at Beth Israel Deaconess Medical Center Mass Spectrometry Core, Harvard Medical School (Boston, MA). 10-15 mg of intestinal samples were grinded in 500 µl of 80% methanol (cooled to -80 °C) for 1-2 min, vortexed for 1 min at 4-8 °C, and incubated at -80 °C for 4 h. The samples were then centrifuged at 14,000 g at 4-8 °C for 10 min. The supernatant was transferred into a new microcentrifuge tube and stored at -80 °C. Four hundred microliters of 80% methanol (cooled to -80 °C) were added to the precipitate, vortexed for 1 min at 4-8 °C, and incubated at -80 °C for 30 min. After incubation, the samples were centrifuged for 10 min at 4-8 °C and the supernatant was collected and mixed with the supernatant extracted in the previous step. The samples were lyophilized using a SpeedVac (SPD121P, Savant, Thermo Fisher Scientific Inc., Billerica, MA) and stored at -80 °C.

Lipid analysis: The lipid analysis [high-performance liquid chromatography (HPLC) and gas chromatography–mass spectrometry (GC/MS) fatty acid methyl esters (FAME) analysis] was performed at the Lipid and Lipid Metabolite Analysis Core at the Women and Children's Health Research Institute of the University of Alberta (Edmonton, Canada). Tissue and serum samples were stored at -80 °C. Hepatic samples were homogenized (LabGEN 700, Cole Parmer North America, Vernon Hills, IL) on ice for 1 min in 1X PBS. Protein concentration of each homogenate was determined using a Bradford assay (BioRad Laboratories, Hercules, CA). Approximately 1 mg of each tissue homogenate and 100 µL of plasma were used per lipid extraction. For each extraction, 50 µg of phosphatidylmonomethylethanolamine (PDME, Avanti Polar Lipids, Alabaster, AL) or 5 µg of C17 FAME were added as an internal standard for HPLC and GC/MS samples respectively. Lipids were extracted using the Folch method. Homogenates were added to a 8:4:3 ratio of chloroform: methanol: water mix, vortexed for 1 min, and centrifuged at 1,800 rpm for 10 min. The bottom phase was transferred to a new 15 ml glass tube. Samples were dried using a thin-stream of nitrogen gas. For the short chain fatty acid (SCFA) analysis, tissue and serum samples were stored at -80 °C. Approximately 500 µL of plasma serum and 60 µg of contents from the colon were packaged on dry ice. Samples were shipped overnight to the Lipidomics Lab at the Nutrition Obesity Research Center of the University of Michigan (Ann Arbor, MI) for lipid extraction and GC-MS analysis of SCFA.

Statistical analysis: Statistical analysis was performed using the SPSS Statistics 20 software (IBM, Armonk, NY) and the Prism 5 GraphPad software (GraphPad Software Inc., La Jolla, CA). Prism 5 was also used for plotting and graphing the data. Data are presented as mean ± SEM (standard error of the mean). For the glucose tolerance test and the insulin tolerance test, the area under the curve (AUC) was calculated, using the trapezoid rule. Means between the experimental conditions were compared using unpaired t test. Differences were considered significant if the probability (P) value was less than 0.05. For correlation analyses, R^2 and the Pearson correlation coefficient were calculated. For the metabolomics studies, data were analyzed using MetaboAnalyst (http://www.metaboanalyst.ca, free online software) *(34)*. For the analysis of the RT-PCR data, relative quantification of gene expression was performed using the comparative Ct method and gene expression fold change was calculated. For each sample, four reference genes were used and the (four) numbers of fold change expression were averaged. Then, one sample t test was used to test whether the change in gene expression was statistically different than 1. The M statistic was used to identify the most stably expressed reference genes and to determine the minimum number of reference genes required *(35)*.

Supplementary Text 1

The intestine is the most vigorously self-renewing tissue of adult mammals. It is considered one of the most energetically costly tissues to maintain, in view of the continuous turnover and shedding of the intestinal epithelium. It needs a disproportionate high amount of energy for its size (the mass of the gastrointestinal tract is about 1 kg in a 65 kg human male). This energy requirement has been estimated to be a striking 15% of the total basal metabolic rate of the body *(36, 37)*. Intestinal energy production is largely derived from glucose and glutamine metabolism.

Previous studies in RYGB-treated rats have shown increased intestinal mass after RYGB *(11, 12, 16)*. We also observed that the intestine of RYGB-treated rats displayed tissue remodeling, characterized by increased intestinal mass due to hyperplasia and hypertrophy after RYGB (figs. S2 to S4). Characteristically, the weight of the Roux limb of RYGB-treated rats ranged from 185 to 330 mg/cm, whereas the weight of the jejunum of sham-operated rats ranged from 80 to 95 mg/cm. This was a 2.5 - 4-fold difference ($P<$ 0.001; unpaired *t* test). We observed intestinal remodeling at all time points studied, that is, 1, 2, and 6 months after RYGB and we found no statistical significant difference in the intestinal weight between these postoperative time points. It is not only an energetically expensive process to build this increased intestinal mass but also an energetically expensive and ongoing effort to sustain this increased mass. Our study shows that the intestine after RYGB enhances its glucose uptake and utilization to meet its increased bioenergetic demands of tissue growth and maintenance, and is turned into a major tissue for glucose disposal, contributing to the RYGB-induced improved glycemic control.

Supplementary Text 2

Our experiments on the nonobese, diabetic models of STZ-induced diabetic and GK rats that had undergone RYGB, are of particular importance in proving a role for reprogramming of intestinal glucose metabolism in the improvement in glycemic control after RYGB, independently of weight loss, improved insulin secretion, or improved insulin sensitivity. RYGB conferred a protective effect and resulted in lower blood glucose levels in comparison with sham operation, in nonobese, diabetic rats in which diabetes was induced by the administration of two different doses (60 or 100 mg/kg) of STZ (Fig. 1B). The blood insulin levels, at 7 days after STZ administration, were less than 100 pmol/l and they were not different between the two comparison groups of STZ-induced diabetic RYGB-treated and sham-operated rats. There was also no difference in the body weight of the animals, as the two groups were matched for body weight at the beginning of the experiment (fig. S1F). The [18F]FDG intestinal uptake was higher and the [18F]FDG blood signal was lower in STZ-induced diabetic RYGB-treated rats in comparison with STZ-induced diabetic sham-operated rats. In view of no statistically significant difference in body weight and blood insulin levels between the RYGB-treated and sham-operated rats, the beneficial effect of RYGB on whole-body glucose disposal, after STZ-induced diabetes, could be attributed to the enhanced intestinal GLUT-1–mediated basolateral glucose uptake and utilization (fig. S8B). Similarly, RYGB-treated GK rats exhibited lower blood glucose levels and better glucose excursion curves after oral glucose administration in comparison with sham-operated GK rats, whereas there was no statistically significant difference in insulin sensitivity test or blood insulin levels between RYGB-treated and sham-operated GK rats (Fig. 1, C and D, and fig. S1, H and I). GK rats also exhibited minimal weight loss after RYGB (fig. S1G). [18F]FDG PET/CT scanning also showed increased intestinal glucose uptake in RYGB-treated GK rats in comparison with sham-operated GK rats. Taken together, these data demonstrate that reprogramming of intestinal glucose metabolism contributes to the improvement in glycemic control after RYGB, independently of weight loss, improved insulin secretion, or improved insulin sensitivity.

Fig. S1

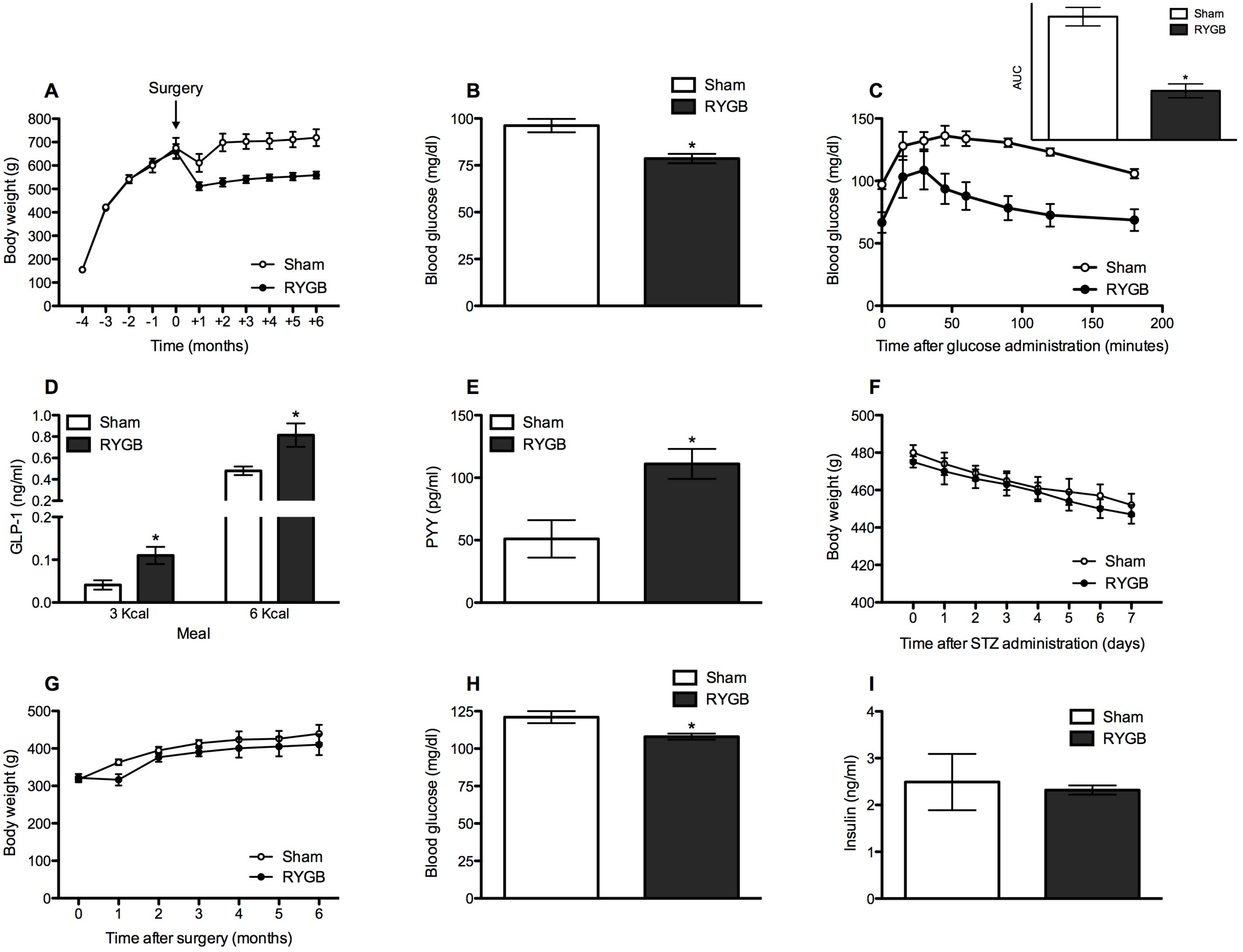
A
Surgery
Body weight (g)
800
700
600
500
400
300
200
100
0
-4
-3
-2
-1
0
+1
+2
+3
+4
+5
+6
Time (months)
Sham
RYGB
B
Sham
RYGB
Blood glucose (mg/dl)
100
75
50
25
0
*
C
AUC
Sham
RYGB
*
Blood glucose (mg/dl)
150
100
50
0
0
50
100
150
200
Time after glucose administration (minutes)
Sham
RYGB
D
GLP-1 (ng/ml)
1.0
0.8
0.6
0.4
0.2
0.2
0.1
0.0
Sham
RYGB
*
*
3 Kcal
6 Kcal
Meal
E
PYY (pg/ml)
150
100
50
0
Sham
RYGB
*
F
Body weight (g)
500
480
460
440
420
400
0
1
2
3
4
5
6
7
Time after STZ administration (days)
Sham
RYGB
G
Body weight (g)
500
400
300
200
100
0
0
1
2
3
4
5
6
Time after surgery (months)
Sham
RYGB
H
Sham
RYGB
Blood glucose (mg/dl)
125
100
75
50
25
0
*
I
Insulin (ng/ml)
4
3
2
1
0
Sham
RYGB

Fig. S1

RYGB induces weight loss and improvement in glucose metabolism. (A) Body weight curves of RYGB-treated and sham-operated DIO rats. RYGB-treated DIO rats exhibited substantial and sustained weight loss. **(B)** Fasting blood glucose levels were lower in RYGB-treated DIO rats. **(C)** RYGB-treated DIO rats exhibited better glucose excursion curves after oral glucose administration. The inset shows the area under the curve (AUC) of the oral glucose tolerance test. **(D)** Postprandial blood glucagon-like peptide 1 (GLP-1) levels were higher in RYGB-treated DIO rats. **(E)** Blood peptide YY (PYY) levels were higher in RYGB-treated DIO rats. **(F)** Body weight curves of RYGB-treated and sham-operated nonobese rats, after the administration of STZ. There was no difference in the body weight curves, as the two groups of RYGB-treated and sham-operated nonobese rats were matched for body weight at the beginning of the experiment of STZ administration. **(G)** Body weight curves of RYGB-treated and sham-operated GK rats. GK rats exhibited minimal weight loss after RYGB. **(H)** Fasting blood glucose levels were lower in RYGB-treated GK rats. **(I)** There was no difference in fasting blood insulin levels between RYGB-treated and sham-operated GK rats. (A) to (E) $N = 7$ to 9 rats; (B) to (E) 1 month postoperatively; (F) to (I) $N = 5$ to 7 rats; (F), (H), and (I) 2 months postoperatively; mean ± SEM; $^*P < 0.05$; unpaired *t* test.

Fig. S2

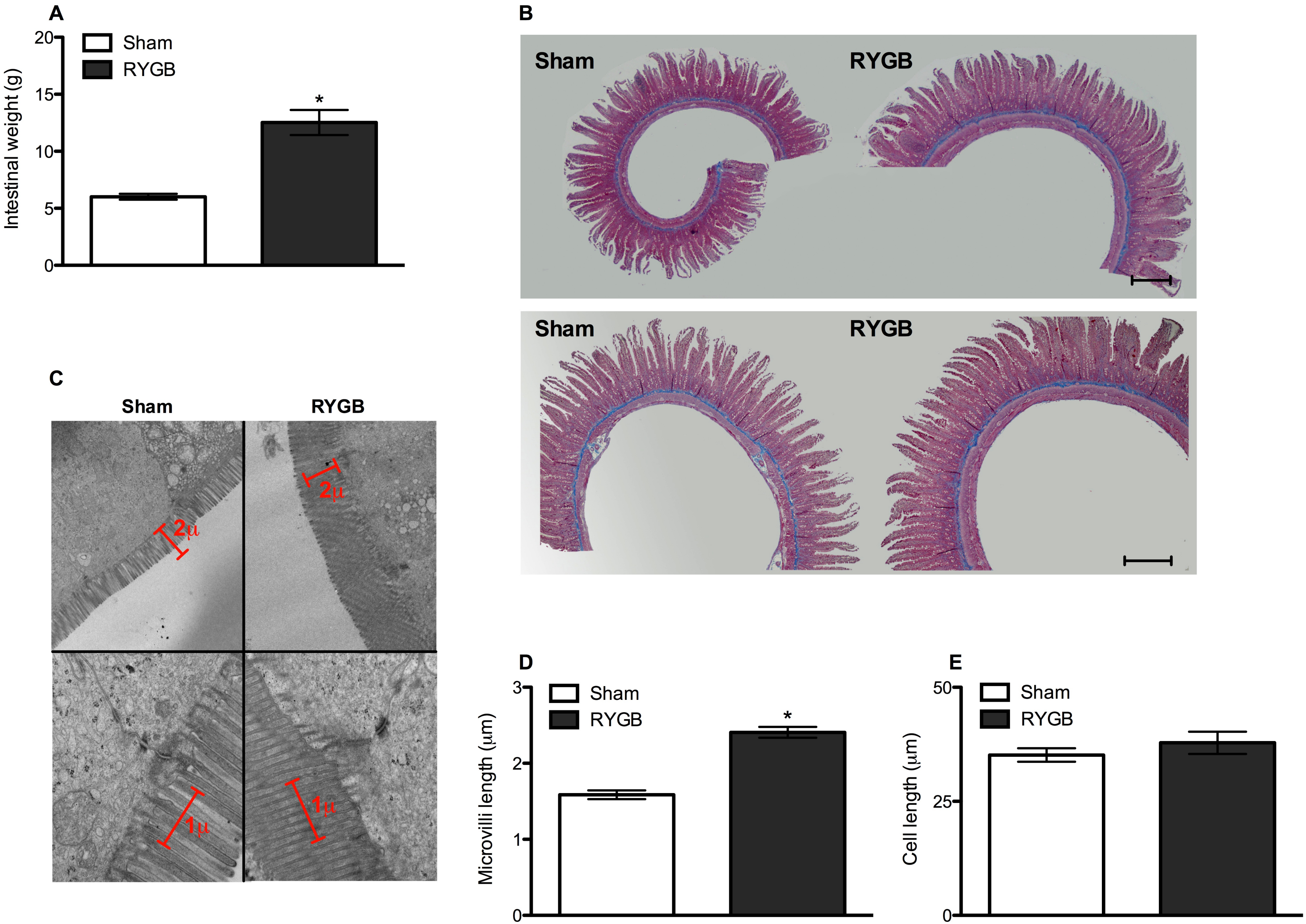
A
Intestinal weight (g)
0
5
10
15
20
Sham
RYGB
*
B
Sham
RYGB
Sham
RYGB
C
Sham
RYGB
2μ
2μ
1μ
1μ
D
Microvilli length (μm)
0
1
2
3
Sham
RYGB
*
E
Cell length (μm)
0
25
50
Sham
RYGB

Fig. S2

RYGB induces intestinal remodeling characterized by increased intestinal mass due to hyperplasia and hypertrophy. (A) RYGB-treated rats exhibited a 2-fold increase in intestinal mass. **(B)** Representative images of Masson's trichrome staining of Roux limb sections of RYGB-treated rats and corresponding jejunal sections of sham-operated rats (scale bar, 500 μm). There was an increase in the density and the width of the villi of the Roux limb. There was also a slight increase in the thickness of the muscular layer of the Roux limb, whereas there was no change in collagen deposition (blue color). Similar changes were observed in the proximal common limb, but to a lesser degree than the Roux limb. **(C** to **E)** Representative images of transmission electron microscopy of the brush border of the Roux limb of RYGB-treated rats and corresponding segments of the jejunum of sham-operated rats. Analysis of the ultrastructure of the intestine showed a 60% increase in the length and density of the microvilli in the Roux limb. The length of the enterocytes was higher in the Roux limb, but the difference did not reach statistical significance. The assessment of cellular length should be interpreted with caution, because it is methodologically difficult to acquire accurate measurements of a 3D structure using 2D images. (A) and (B) $N = 7$ to 9 rats, 2 months postoperatively; the results were reproduced at 1 and 6 months postoperatively; (C) to (E) $N = 5$ rats, 2 months postoperatively; mean ± SEM; $^{*}P < 0.05$; unpaired t test.

Fig. S3

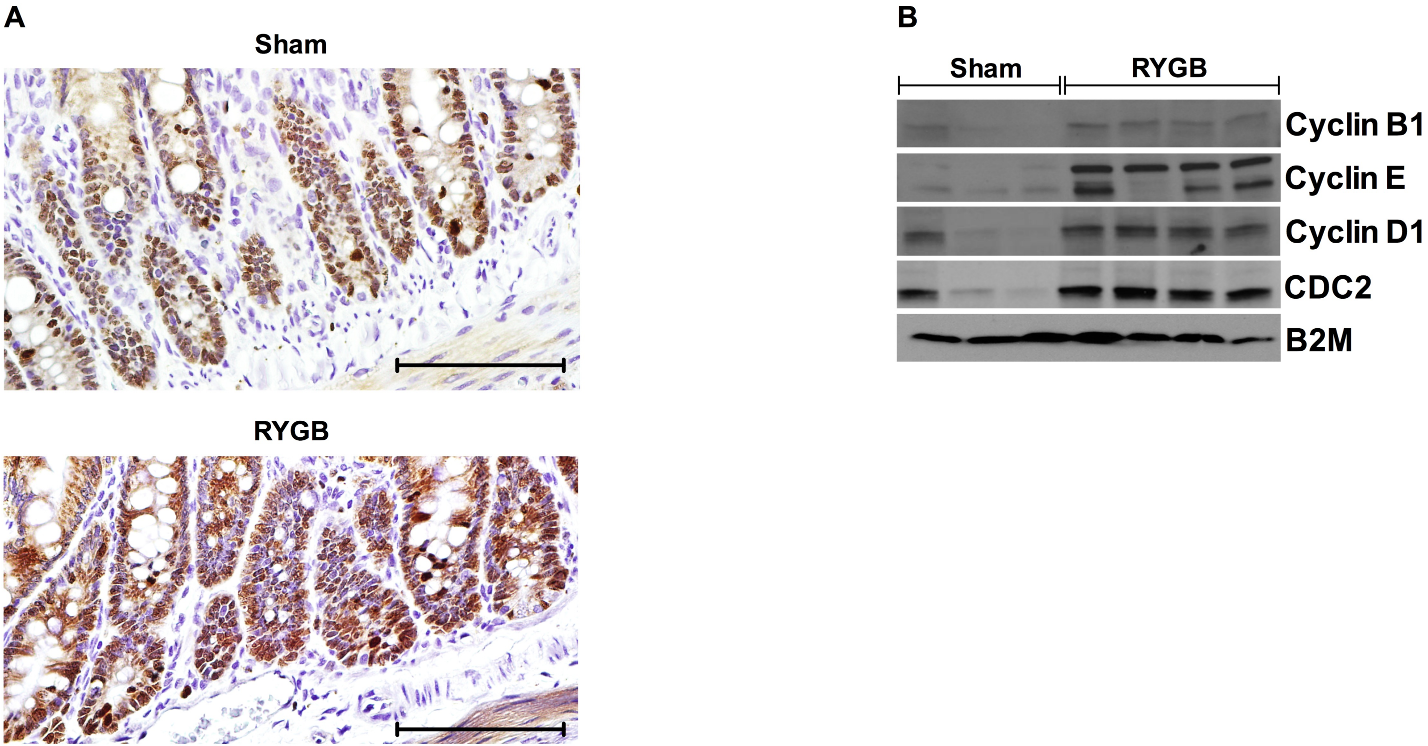

Fig. S3

RYGB induces intestinal remodeling. (A) Representative images of Roux limb sections of RYGB-treated rats and corresponding jejunal sections of sham-operated rats stained with an antibody against Ki-67, a cellular proliferation marker (scale bar, 100 µm). Ki-67 expression was increased in the Roux limb. **(B)** Consistent with increased cellular proliferation, the protein levels of several cyclins (B1, E, and D1) and cyclin-dependent kinase 1 (CDC2) were increased in the Roux limb of RYGB-treated rats. (A) and (B) $N =$ 7 to 9 rats, 2 months postoperatively.

Fig. S4

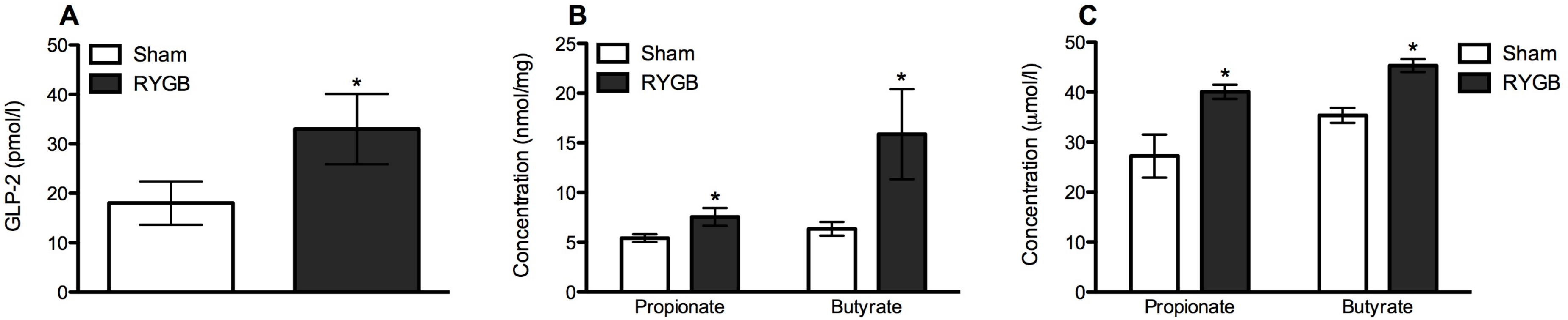

A
GLP-2 (pmol/l)
50
40
30
20
10
0
Sham
RYGB
*
B
Concentration (nmol/mg)
25
20
15
10
5
0
Sham
RYGB
*
*
Propionate
Butyrate
C
Concentration (µmol/l)
50
40
30
20
10
0
Sham
RYGB
*
*
Propionate
Butyrate

Fig. S4

RYGB induces factors that promote intestinal remodeling. (A) Blood glucagon-like peptide 2 (GLP-2) levels were higher in RYGB-treated rats. **(B)** Intestinal luminal contents of butyrate and propionate, two short chain fatty acids (SCFA), were higher in RYGB-treated rats. **(C)** Blood levels of butyrate and propionate were higher in RYGB-treated rats. The increased levels of GLP-2 and SCFA could promote the morphological adaptation, characterized by hyperplasia and hypertrophy, of the Roux limb and the proximal common limb, and could also explain the lack of atrophy of the biliopancreatic limb of RYGB-treated rats. (A) to (C) $N = 7$ to 9 rats, 2 months postoperatively; mean ± SEM; $*P < 0.05$; unpaired t test.

Fig. S5

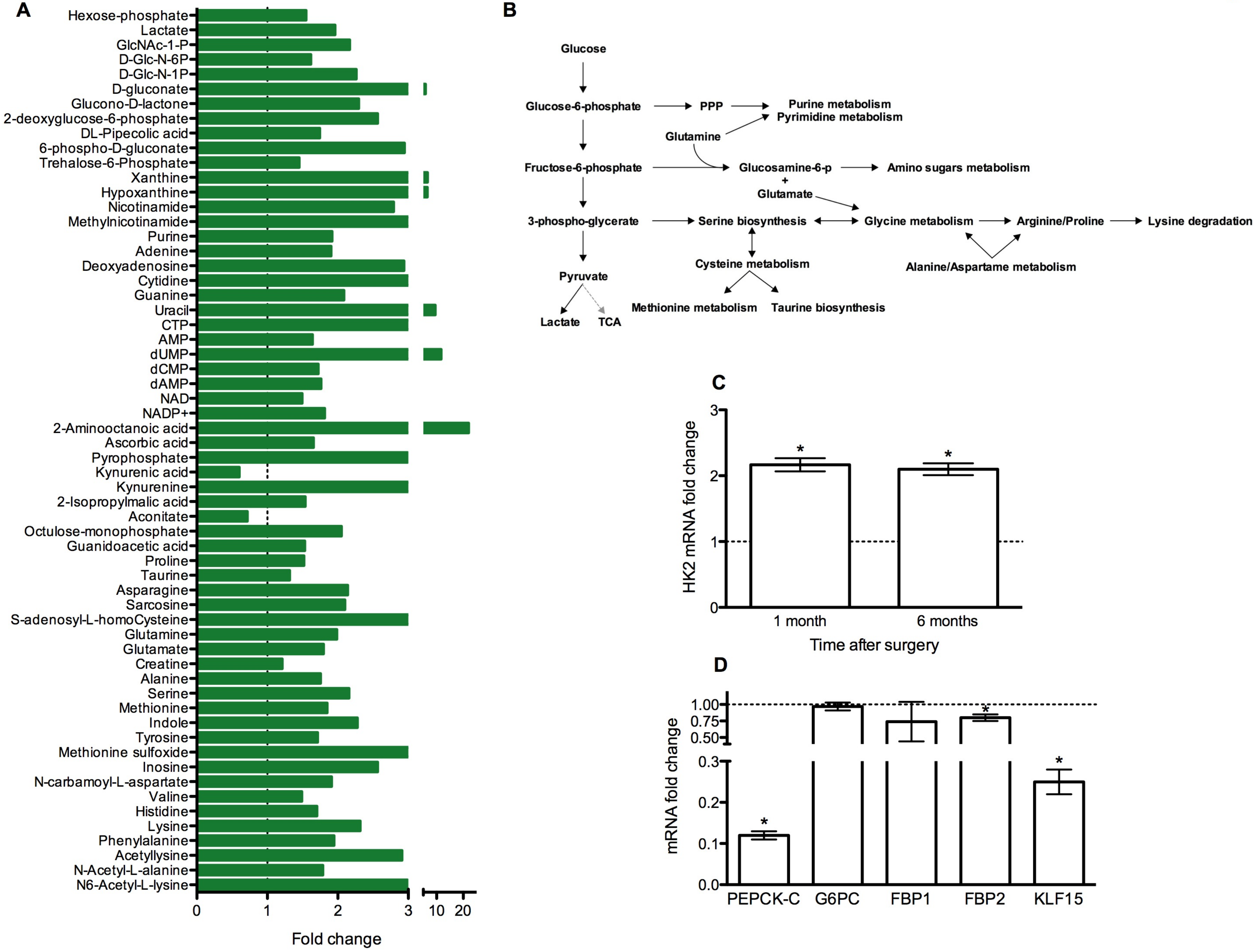
A
Hexose-phosphate
Lactate
GlcNAc-1-P
D-Glc-N-6P
D-Glc-N-1P
D-gluconate
Glucono-D-lactone
2-deoxyglucose-6-phosphate
DL-Pipecolic acid
6-phospho-D-gluconate
Trehalose-6-Phosphate
Xanthine
Hypoxanthine
Nicotinamide
Methylnicotinamide
Purine
Adenine
Deoxyadenosine
Cytidine
Guanine
Uracil
CTP
AMP
dUMP
dCMP
dAMP
NAD
NADP+
2-Aminooctanoic acid
Ascorbic acid
Pyrophosphate
Kynurenic acid
Kynurenine
2-Isopropylmalic acid
Aconitate
Octulose-monophosphate
Guanidoacetic acid
Proline
Taurine
Asparagine
Sarcosine
S-adenosyl-L-homoCysteine
Glutamine
Glutamate
Creatine
Alanine
Serine
Methionine
Indole
Tyrosine
Methionine sulfoxide
Inosine
N-carbamoyl-L-aspartate
Valine
Histidine
Lysine
Phenylalanine
Acetyllysine
N-Acetyl-L-alanine
N6-Acetyl-L-lysine
0
1
2
3
10
20
Fold change
B
Glucose
Glucose-6-phosphate
PPP
Purine metabolism
Pyrimidine metabolism
Glutamine
Fructose-6-phosphate
Glucosamine-6-p
+
Glutamate
Amino sugars metabolism
3-phospho-glycerate
Serine biosynthesis
Glycine metabolism
Arginine/Proline
Lysine degradation
Alanine/Aspartame metabolism
Cysteine metabolism
Methionine metabolism
Taurine biosynthesis
Pyruvate
Lactate
TCA
C
HK2 mRNA fold change
0
1
2
3
*
*
1 month
6 months
Time after surgery
D
mRNA fold change
1.00
0.75
0.50
0.3
0.2
0.1
0.0
*
*
*
PEPCK-C
G6PC
FBP1
FBP2
KLF15

Fig. S5

RYGB induces reprogramming of intestinal glucose metabolism. (A) List of metabolites, derived from the metabolomic profiling, with statistically significant changes in the Roux limb of RYGB-treated rats in comparison with corresponding segments of the jejunum of sham-operated rats. **(B)** The schematic diagram presents the most important metabolic pathways involved in glucose utilization in the Roux limb of RYGB-treated rats. **(C)** RNA levels of HK2 were increased at 1 and 6 months postoperatively in the Roux limb of RYGB-treated rats. **(D)** Consistent with the reciprocal regulation of glycolysis and gluconeogenesis, RNA levels of phosphoenolpyruvate carboxykinase 1 (PEPCK-C), fructose-1,6-bisphosphatase 2 (FBP2), and Krüppel-like factor 15 (KLF15) were decreased in the Roux limb of RYGB-treated rats. There was no difference in RNA levels of glucose-6-phosphatase (G6PC) and fructose-1,6-bisphosphatase 1 (FBP1). (A) $N = 6$ rats, 2 months postoperatively; (C) and (D) $N = 7$ to 9 rats; (D) 2 months postoperatively; the results were reproduced at 1 and 6 months postoperatively; mean ± SEM; $^*P < 0.05$; (A) unpaired *t* test; (C) and (D) one sample *t* test.

Fig. S6

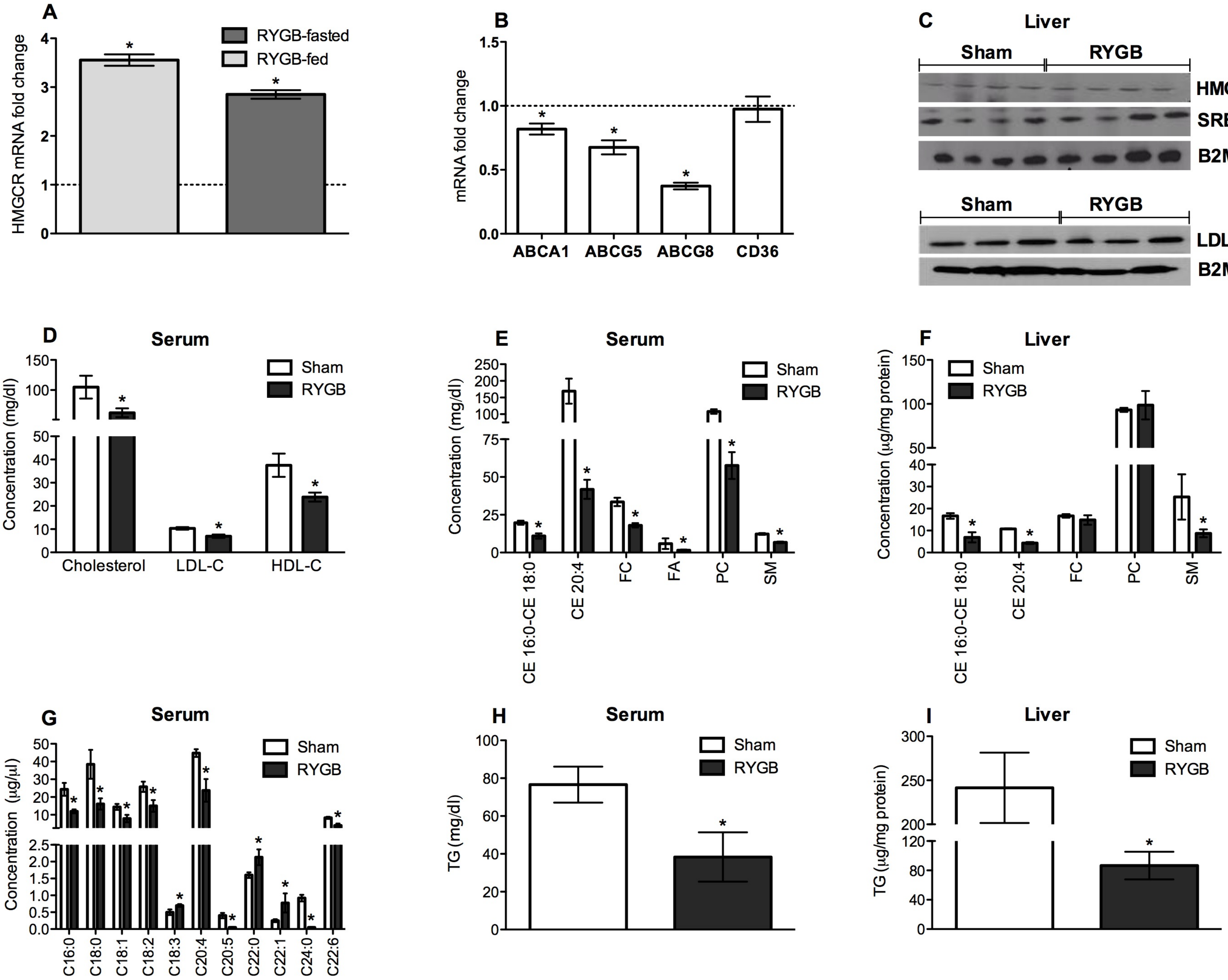
A
HMGCR mRNA fold change
4
3
2
1
0
RYGB-fasted
RYGB-fed
*
*
B
mRNA fold change
1.5
1.0
0.5
0.0
ABCA1
ABCG5
ABCG8
CD36
*
*
*
C
Liver
Sham
RYGB
HMGCR
SREBP2
B2M
Sham
RYGB
LDLR
B2M
D
Serum
Concentration (mg/dl)
150
100
50
40
30
20
10
0
Sham
RYGB
Cholesterol
LDL-C
HDL-C
*
*
*
E
Serum
Concentration (mg/dl)
250
200
150
100
75
50
25
0
Sham
RYGB
CE 16:0-CE 18:0
CE 20:4
FC
FA
PC
SM
*
*
*
*
*
*
F
Liver
Concentration (μg/mg protein)
150
100
50
40
30
20
10
0
Sham
RYGB
CE 16:0-CE 18:0
CE 20:4
FC
PC
SM
*
*
*
G
Serum
Concentration (μg/μl)
50
40
30
20
10
2.5
2.0
1.5
1.0
0.5
0.0
Sham
RYGB
C16:0
C18:0
C18:1
C18:2
C18:3
C20:4
C20:5
C22:0
C22:1
C24:0
C22:6
*
H
Serum
TG (mg/dl)
100
80
60
40
20
0
Sham
RYGB
*
I
Liver
TG (μg/mg protein)
300
250
200
120
80
40
0
Sham
RYGB
*

Fig. S6

(A to C) RYGB increases intestinal cholesterol requirements. (A) RNA levels of HMGCR were increased in the Roux limb of fasted and fed RYGB-treated rats. **(B)** RNA levels of ATP-binding cassette transporter 1 (ABCA1), ATP-binding cassette sub-family G member 5 (ABCG5), and ATP-binding cassette sub-family G member 8 (ABCG8) were decreased in the Roux limb of RYGB-treated rats. There was no difference in RNA levels of cluster of differentiation 36 (CD36). These data suggest that trans-intestinal cholesterol efflux may be decreased in the Roux limb of RYGB-treated rats, most likely as an effort of the intestine to support its increased cholesterol requirements. **(C)** There was no difference in the protein levels of factors involved in hepatic cholesterol biosynthesis and uptake between RYGB-treated and sham-operated rats. **(D to I) RYGB induces improvement in serum and hepatic lipid profiles. (D)** Serum total cholesterol, low-density lipoprotein cholesterol (LDL-C), and high-density lipoprotein cholesterol (HDL-C) levels were lower in RYGB-treated rats. **(E)** Serum levels of 16:0, 18:0, and 20:4 cholesteryl ester (CE), free cholesterol (FC), fatty acids (FA), phosphatidylcholine (PC), and sphingomyelin (SM) were lower in RYGB-treated rats. **(F)** Hepatic levels of 16:0, 18:0, and 20:4 CE, and SM were lower in RYGB-treated rats. **(G)** Serum levels of most fatty acid fractions measured were lower in RYGB-treated rats. C16:0, palmitic acid; C18:0, stearic acid; C18:1, vaccenic acid; C18:2, linoleic acid; C18:3, alpha-linolenic acid; C20:4, arachidonic acid; C20:5, eicosapentaenoic acid; C22:0, behenic acid; C22:1, erucic acid; C24:0, lignoceric acid; C22:6, docosahexaenoic acid. **(H)** Serum levels of triglycerides (TG) were lower in RYGB-treated rats. **(I)** Hepatic levels of TG were lower in RYGB-treated rats. (A) to (I) $N = 7$ to 9 rats, 2 months postoperatively;

mean ± SEM; $^*P < 0.05$; (A) and (B) one sample t test; (D) to (I) unpaired t test.

Fig. S7

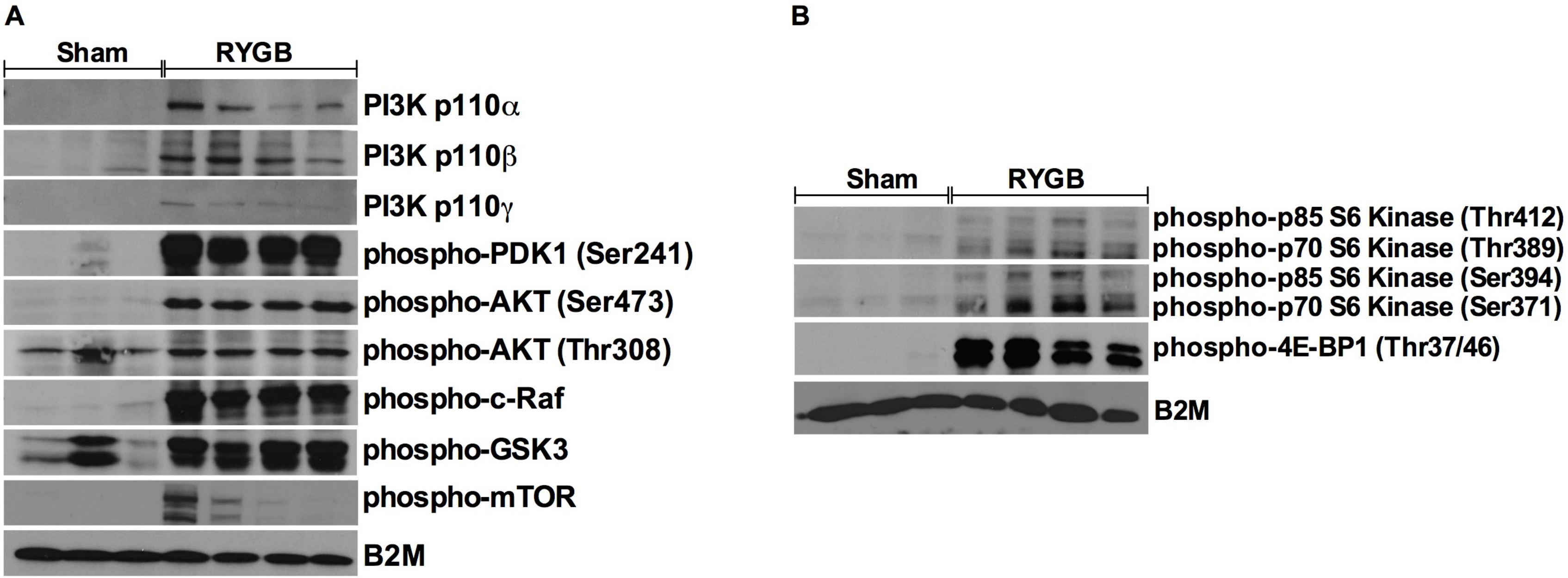
A
Sham
RYGB
PI3K p110α
PI3K p110β
PI3K p110γ
phospho-PDK1 (Ser241)
phospho-AKT (Ser473)
phospho-AKT (Thr308)
phospho-c-Raf
phospho-GSK3
phospho-mTOR
B2M
B
Sham
RYGB
phospho-p85 S6 Kinase (Thr412)
phospho-p70 S6 Kinase (Thr389)
phospho-p85 S6 Kinase (Ser394)
phospho-p70 S6 Kinase (Ser371)
phospho-4E-BP1 (Thr37/46)
B2M

Fig. S7

(A and **B) PI3K/AKT/mTOR pathway was activated in the Roux limb of RYGB-treated rats.** PI3K, phosphoinositide 3-kinase; mTOR, mammalian target of rapamycin; PDK1, 3-phosphoinositide dependent protein kinase-1; GSK3, glycogen synthase kinase-3; 4E-BP1, eukaryotic translation initiation factor-4E-binding protein-1. (A) and (B) $N =$ 7 to 9 rats, 2 months postoperatively.

Fig. S8

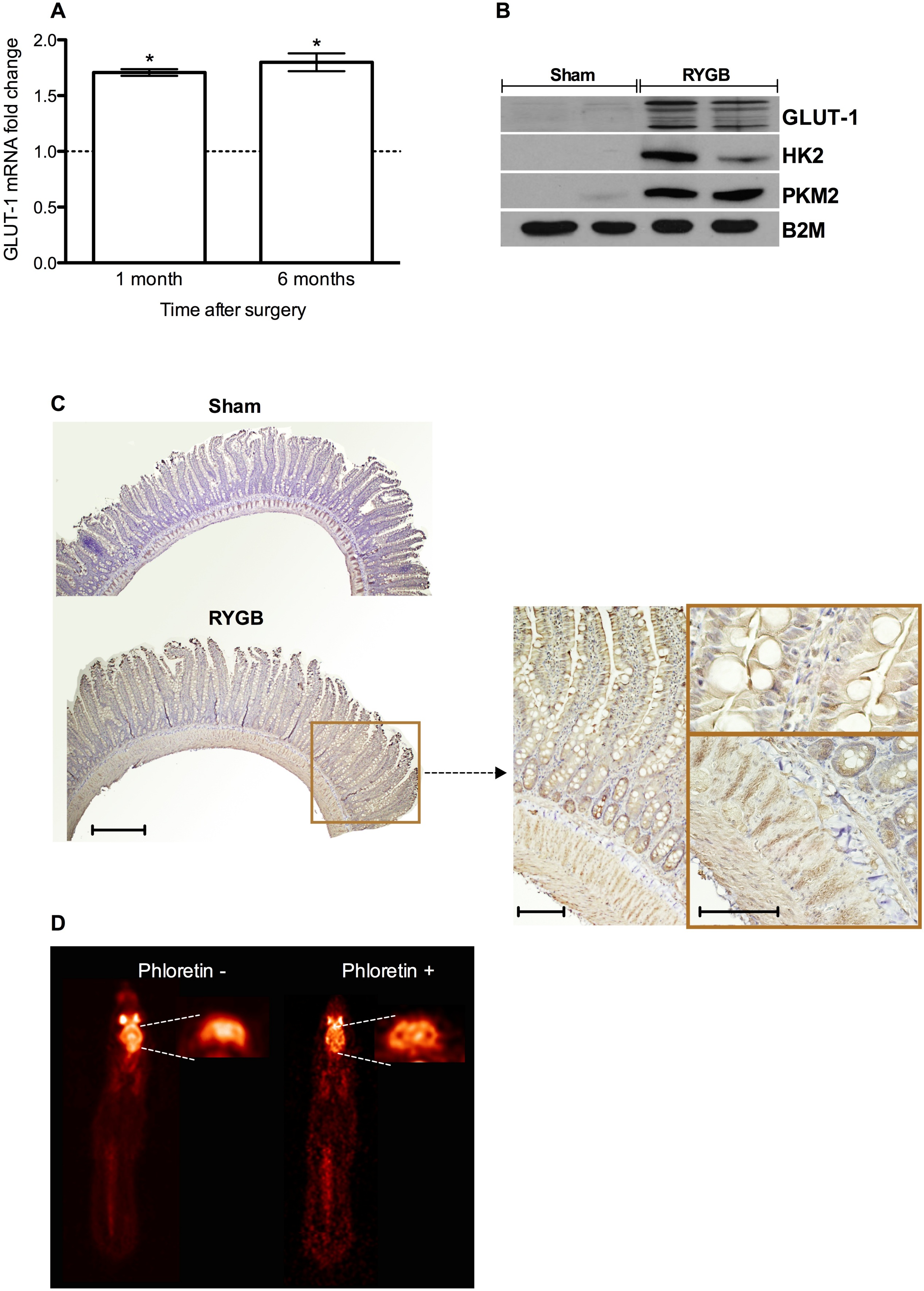
A
GLUT-1 mRNA fold change
2.0
1.5
1.0
0.5
0.0
*
*
1 month
6 months
Time after surgery
B
Sham
RYGB
GLUT-1
HK2
PKM2
B2M
C
Sham
RYGB
D
Phloretin -
Phloretin +

Fig. S8

RYGB enhances intestinal GLUT-1–mediated basolateral glucose uptake and utilization. (A) GLUT-1 RNA levels were increased at 1 and 6 months postoperatively in the Roux limb of RYGB-treated rats. **(B)** GLUT-1, HK2, and PKM2 protein levels were increased in the Roux limb of STZ-induced diabetic rats that had undergone RYGB. **(C)** Representative images of Roux limb sections of RYGB-treated rats and corresponding jejunal sections of sham-operated rats stained with an antibody against GLUT-1. GLUT-1 expression was increased in the Roux limb of RYGB-treated rats (left) (scale bar, 500 μm). GLUT-1 expression was higher in the villi (upper right), the crypt cells, and the muscular layer (lower right) of the Roux limb (scale bar, 100 μm). **(D)** Representative images of whole-body [18F]FDG PET/CT scanning, with or without the administration of phloretin, a GLUT-1 inhibitor. The blocking effect of phloretin on GLUT-1 was confirmed by analyzing the PET/CT scan images of the brain that showed a substantial decrease in the intensity of the [18F]FDG signal after the administration of phloretin. (A), (C), and (D) $N = 7$ to 9 rats; (B) $N = 5$ to 7 rats, 2 months postoperatively; (C) 2 months postoperatively; the results were reproduced at 1 and 6 months postoperatively; (D) 6 months postoperatively; $^{*}P < 0.05$; one sample *t* test.

Fig. S9

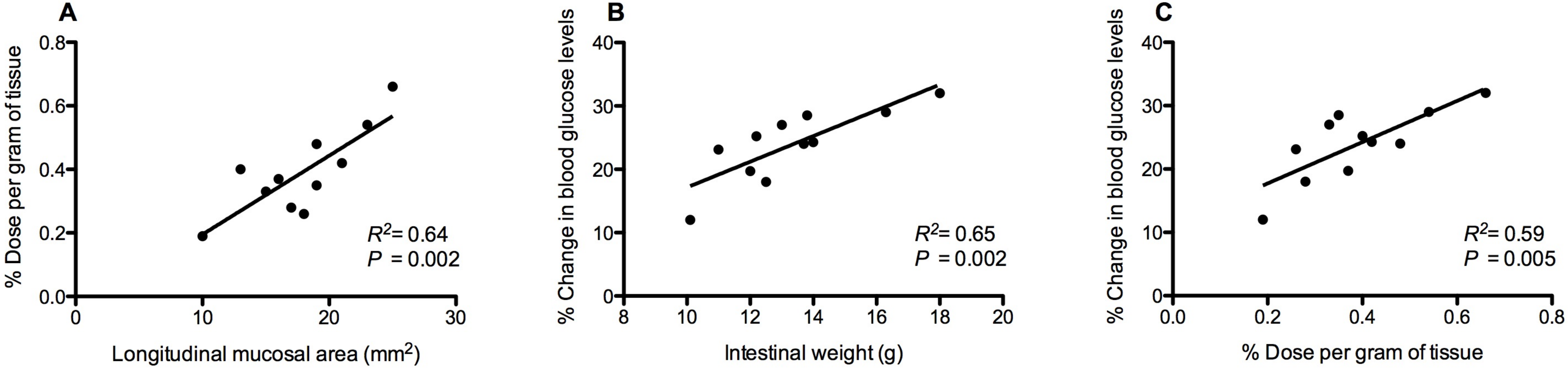
A
% Dose per gram of tissue
0.8
0.6
0.4
0.2
0.0
0
10
20
30
Longitudinal mucosal area (mm²)
R² = 0.64
P = 0.002
B
% Change in blood glucose levels
40
30
20
10
0
8
10
12
14
16
18
20
Intestinal weight (g)
R² = 0.65
P = 0.002
C
% Change in blood glucose levels
40
30
20
10
0
0.0
0.2
0.4
0.6
0.8
% Dose per gram of tissue
R² = 0.59
P = 0.005

Fig. S9

RYGB enhances intestinal GLUT-1–mediated basolateral glucose uptake and utilization, which contributes to the improvement in glycemic control. **(A)** The variability in the glucose uptake by the intestine of RYGB-treated rats correlated statistically significantly with the degree of intestinal remodeling of the Roux limb. The variability in the longitudinal mucosal area of the Roux limb of RYGB-treated rats could explain 64% of the variability in the intestinal glucose uptake. **(B)** There was a statistically significant correlation between the intestinal mass of RYGB-treated rats and the percent change in their blood glucose levels before and after RYGB treatment. **(C)** There was a statistically significant correlation between the glucose uptake by the intestine of RYGB-treated rats and the percent change in their blood glucose levels before and after RYGB treatment. (A) to (C) $N = 11$ rats, 6 months postoperatively.

Fig. S10

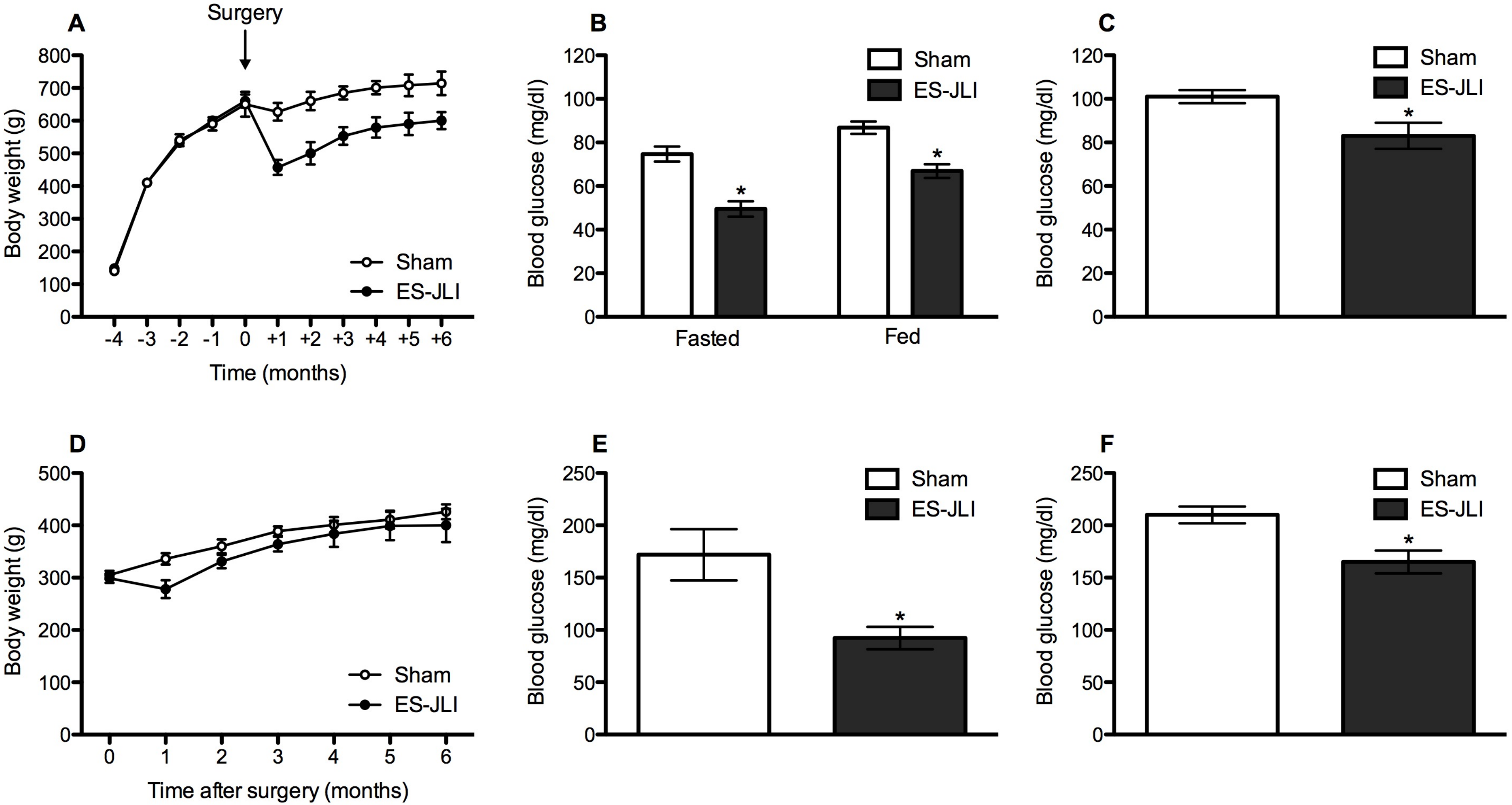
A
Surgery
Body weight (g)
800
700
600
500
400
300
200
100
0
-4
-3
-2
-1
0
+1
+2
+3
+4
+5
+6
Time (months)
Sham
ES-JLI
B
Blood glucose (mg/dl)
120
100
80
60
40
20
0
Fasted
Fed
Sham
ES-JLI
*
*
C
Blood glucose (mg/dl)
120
100
80
60
40
20
0
Sham
ES-JLI
*
D
Body weight (g)
500
400
300
200
100
0
0
1
2
3
4
5
6
Time after surgery (months)
Sham
ES-JLI
E
Blood glucose (mg/dl)
250
200
150
100
50
0
Sham
ES-JLI
*
F
Blood glucose (mg/dl)
250
200
150
100
50
0
Sham
ES-JLI
*

Fig. S10

ES-JLI induces weight loss and improvement in glucose metabolism. (A) Body weight curves of ES-JLI–treated and sham-operated DIO rats. ES-JLI–treated DIO rats exhibited substantial and sustained weight loss. **(B)** Blood glucose levels were lower in fasted and fed ES-JLI–treated DIO rats at 1 month postoperatively. **(C)** Fasting blood glucose levels were lower in ES-JLI–treated DIO rats at 6 months postoperatively. **(D)** Body weight curves of ES-JLI–treated and sham-operated GK rats. GK rats exhibited minimal weight loss after ES-JLI. **(E)** Blood glucose levels were lower in fed ES-JLI–treated GK rats at 1 month postoperatively. **(F)** Blood glucose levels were lower in fed ES-JLI–treated GK rats at 6 months postoperatively. (A) to (F) $N = 5$ to 7 rats; mean ± SEM; $^*P < 0.05$; unpaired t test.

Fig. S11

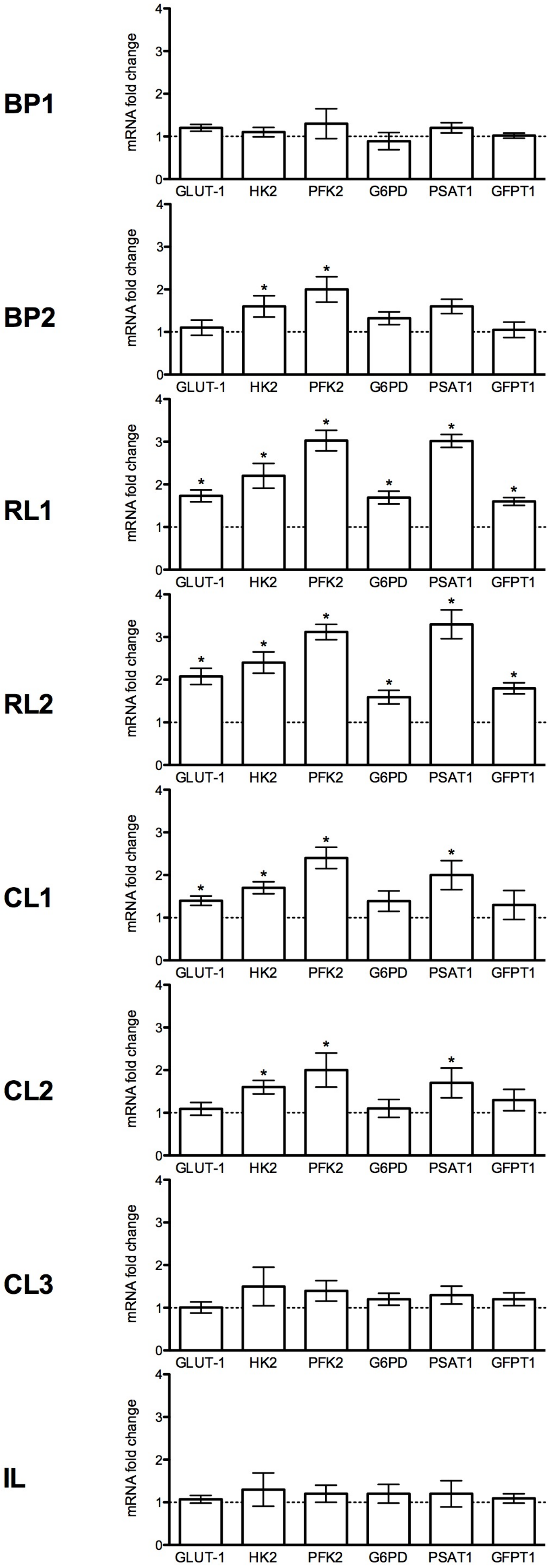
BP1
BP2
RL1
RL2
CL1
CL2
CL3
IL
mRNA fold change
0
1
2
3
4
GLUT-1
HK2
PFK2
G6PD
PSAT1
GFPT1
*

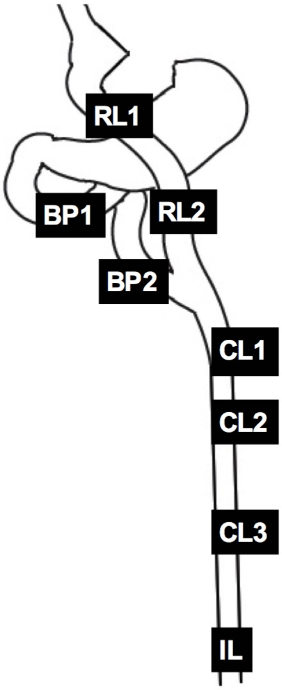
RL1
BP1
RL2
BP2
CL1
CL2
CL3
IL

Fig. S11

A gradient in the change in gene expression levels of key factors and enzymes involved in glucose uptake and utilization is observed along the altered nutrient flow path in the intestine after RYGB. We compared RNA levels of key factors and enzymes involved in glucose uptake and utilization between the various intestinal segments of RYGB-treated rats and corresponding segments of the intestine of sham-operated rats. To characterize the gradient in the change in RNA levels of key factors and enzymes involved in glucose uptake and utilization in more detail, the biliopancreatic limb (BP) and the Roux limb (RL) were studied after being divided in a proximal and distal segment (BP1, BP2 and RL1, RL2) and the common limb (CL) was studied after being divided in four segments, with ileum (IL) being the last (CL1, CL2, CL3, IL). The highest increase in RNA levels of key factors and enzymes involved in glucose uptake and utilization was observed in the Roux limb, which is exposed to undigested nutrients. Lesser increase in RNA levels was observed in the proximal common limb (CL1, CL2), but no change was found in the distal common limb (CL3, IL). The common limb is exposed to a mixture of nutrients with the gastric, hepatic and pancreatic secretions. This difference in the change in RNA levels of key factors and enzymes involved in glucose uptake and utilization between the proximal common limb and the distal common limb could be due to the exposure of the proximal common limb to partially digested nutrients and the exposure of the distal common limb to fully digested nutrients. No change in RNA levels was found in the biliopancreatic limb, which is exposed to the gastric, hepatic and pancreatic secretions but no nutrients. The change observed in RNA levels of HK2 and PFK2 in the distal segment of the biliopancreatic limb (BP2) could be explained by the proximity of this segment to its junction with the Roux limb and the limited retrograde flow that occurs in surgical anastomoses. GLUT-1, glucose transporter-1, this transporter mediates glucose uptake and has a high affinity for glucose. It is normally minimally expressed in the adult intestine but was found to be highly up-regulated in the Roux limb of RYGB-treated rats; HK2, hexokinase 2, this is a critical enzyme that phosphorylates glucose and converts it to glucose-6-phosphate. Cell membrane is impermeable to glucose-6-phosphate, so hexokinase enables more glucose entry into the cell, “traps” glucose, and directs it to downstream metabolic pathways; PFK2, phosphofructokinase 2, this enzyme regulates the rate-limiting step of glycolysis; G6PD, glucose-6-phosphate dehydrogenase, this is the rate-limiting enzyme of the pentose phosphate pathway; PSAT1, phosphoserine aminotransferase-1, this is an enzyme of the serine biosynthetic pathway. The serine biosynthetic pathway branches off from glycolysis and serves as important energy and carbon source; GFPT1, glucosamine-fructose-6-phosphate aminotransferase-1, this enzyme catalyzes the formation of glucosamine 6-phosphate and is the first and rate-limiting enzyme of the hexosamine biosynthetic pathway that provides hexosamine, which is important for sufficient growth factor signaling and glutamine uptake to support cellular growth. $N = 7$ to 9 rats, 6 months postoperatively; mean ± SEM; $^*P < 0.05$; one sample t test.

Fig. S12

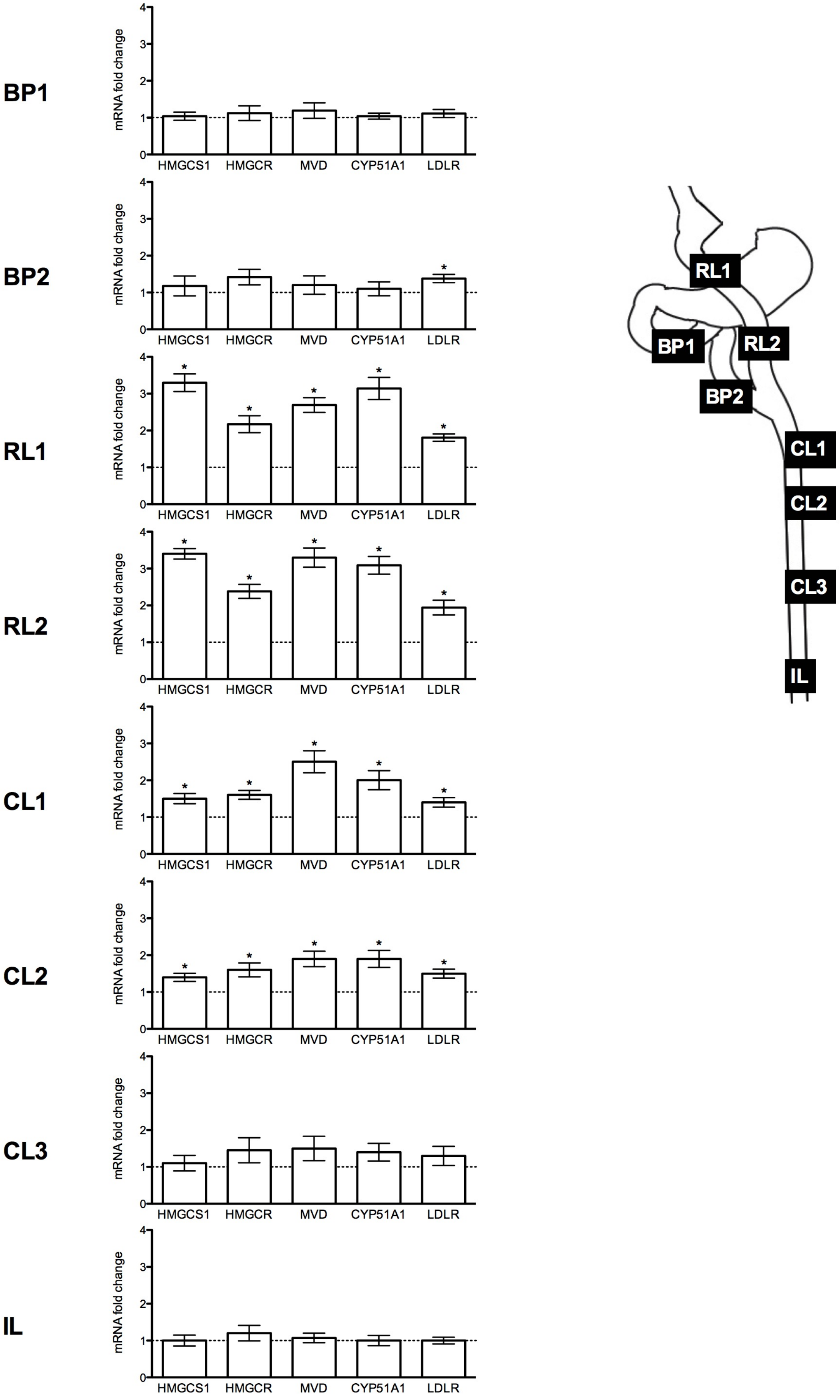
BP1
BP2
RL1
RL2
CL1
CL2
CL3
IL
mRNA fold change
0
1
2
3
4
HMGCS1
HMGCR
MVD
CYP51A1
LDLR
*
RL1
BP1
RL2
BP2
CL1
CL2
CL3
IL

Fig. S12

A gradient in the change in gene expression levels of key factors and enzymes involved in cholesterol biosynthesis and uptake is observed along the altered nutrient flow path in the intestine after RYGB. We compared RNA levels of key factors and enzymes involved in cholesterol biosynthesis and uptake between the various intestinal segments of RYGB-treated rats and corresponding segments of the intestine of sham-operated rats. To characterize the gradient in the change in RNA levels of key factors and enzymes involved in cholesterol biosynthesis and uptake in more detail, the biliopancreatic limb (BP) and the Roux limb (RL) were studied after being divided in a proximal and distal segment (BP1, BP2 and RL1, RL2) and the common limb (CL) was studied after being divided in four segments, with ileum (IL) being the last (CL1, CL2, CL3, IL). The highest increase in RNA levels of key factors and enzymes involved in cholesterol biosynthesis and uptake was observed in the Roux limb, which is exposed to undigested nutrients. Lesser increase in RNA levels was observed in the proximal common limb (CL1, CL2), but no change was found in the distal common limb (CL3, IL). The common limb is exposed to a mixture of nutrients with the gastric, hepatic and pancreatic secretions. This difference in the change in RNA levels of key factors and enzymes involved in cholesterol biosynthesis and uptake between the proximal common limb and the distal common limb could be due to the exposure of the proximal common limb to partially digested nutrients and the exposure of the distal common limb to fully digested nutrients. No change in RNA levels was found in the biliopancreatic limb, which is exposed to the gastric, hepatic and pancreatic secretions but no nutrients. The change observed in RNA levels of LDLR in the distal segment of the biliopancreatic limb (BP2) could be explained by the proximity of this segment to its junction with the Roux limb and the limited retrograde flow that occurs in surgical anastomoses. HMGCS1, 3-hydroxy-3-methylglutaryl-CoA (HMG-CoA) synthase, it catalyzes the reaction in which acetyl-CoA condenses with acetoacetyl-CoA to form HMG-CoA. HMG-CoA is an intermediate in cholesterol biosynthesis; HMGCR, 3-hydroxy-3-methylglutaryl-CoA reductase, this is the rate-limiting enzyme of the metabolic pathway for biosynthesis of cholesterol and other isoprenoids; MVD, mevalonate (diphospho) decarboxylase, this enzyme catalyzes the conversion of mevalonate pyrophosphate into isopentenyl pyrophosphate in one of the early steps in cholesterol biosynthesis; CYP51A1, cytochrome P450, family 51, subfamily A, polypeptide 1 (lanosterol 14-α demethylase), it is part of the cholesterol biosynthesis pathway; LDLR, low-density lipoprotein receptor, this receptor mediates the endocytosis of low-density lipoprotein cholesterol. $N = 7$ to 9 rats, 6 months postoperatively; mean ± SEM; $^*P < 0.05$; one sample t test.

Table S1

Metabolomic profiling of the Roux limb of RYGB-treated rats and corresponding segments of the jejunum of sham-operated rats. Full list of metabolites and their fold change in the Roux limb of RYGB-treated rats in comparison with corresponding segments of the jejunum of sham-operated rats.

Metabolite	**Fold change**	***P* value**
N-acetyl-glucosamine-1-phosphate	2.1672	1.83E-04
Proline	1.5195	7.47E-04
Taurine	1.315	7.47E-04
Asparagine	2.1406	9.48E-04
Sarcosine	2.0994	9.94E-04
S-adenosyl-L-homoCysteine	4.0835	0.0012465
Shikimate	9.5925	0.001372
Glutamine	1.9853	0.0017246
2-Aminooctanoic acid	22.036	0.0023485
dCMP	1.722	0.0025623

Alanine	1.7546	0.0030656
Creatine	1.2101	0.003838
Ascorbic acid	1.6532	0.004781
Pyroglutamic acid	2.7397	0.0049757
Glutamate	1.7968	0.0049928
Pyrophosphate	2.9887	0.0052427
Serine	2.1586	0.0058161
DL-Pipecolic acid	1.7428	0.0061828
Lactate	1.9598	0.0077325
Methylnicotinamide	3.9482	0.0091977
Methionine	1.8478	0.010272
Indole	2.2779	0.01129
Tyrosine	1.7119	0.011745
Methionine sulfoxide	3.1519	0.011977
Inosine	2.5653	0.014166
Glucono-D-lactone	2.2955	0.014872
CTP	3.1593	0.015478

2-deoxyglucose-6-phosphate	2.5644	0.01768
NADP+	1.8127	0.017957
N-Acetyl-L-alanine	1.7861	0.018451
AMP	1.6401	0.018876
N-carbamoyl-L-aspartate	1.9119	0.019672
6-phospho-D-gluconate	2.9459	0.020174
dUMP	11.701	0.02172
N6-Acetyl-L-lysine	2.9868	0.023205
Deoxyadenosine	2.9371	0.023646
Purine	1.9171	0.024115
Adenine	1.903	0.024575
Lysine	2.3169	0.02521
Octulose-monophosphate	2.0503	0.025233
Guanidoacetic acid	1.5313	0.025981
Hexose-phosphate	1.55	0.026128
Kynurenine	3.11	0.030689
2-Isopropylmalic acid	1.5382	0.031387

dAMP	1.761	0.031774
D-gluconate	5.8308	0.031788
D-glucosamine-6-phosphate	1.6158	0.033153
Cytidine	3.7133	0.033986
Valine	1.4877	0.034305
Kynurenic acid	0.60132	0.035407
Guanine	2.0851	0.036383
Phenylalanine	1.9453	0.036922
D-glucosamine-1-phosphate	2.26	0.038404
Acetyllysine	2.9096	0.039169
Uracil	9.5025	0.040285
Trehalose-6-Phosphate	1.4516	0.040656
Histidine	1.7033	0.042169
Xanthine	6.555	0.042227
Nicotinamide	2.7914	0.044932
Hypoxanthine	6.5215	0.04622
Aconitate	0.71594	0.046792

Nicotinamide adenine dinucleotide	1.4938	0.047001
L-Leucine	1.7619	0.052955
Phenylpropiolic acid	1.6853	0.053719
Threonine	1.7988	0.054802
Hydroxyproline	2.2078	0.058353
4-aminobutyrate	2.6419	0.060319
Xanthosine	7.9096	0.060576
Acetylcarnitine DL	1.1914	0.061532
S-ribosyl-L-homocysteine	0.35218	0.062933
Uridine	3.1762	0.063988
Octulose-1,8-bisphosphate	1.7442	0.064132
S-adenosyl-L-methionine	1.9751	0.07084
Methylcysteine	1.6938	0.07217
Ornithine	2.3475	0.072276
Pyridoxamine	2.9483	0.078605
L-arginino-succinate	1.6013	0.080817
Cholic acid	5.0901	0.085242

Glycerophosphocholine	1.0968	0.08554
1-Methyladenosine	2.0319	0.08632
GMP	1.8422	0.086569
Ng,NG-dimethyl-L-arginine	2.0906	0.093386
CMP	1.392	0.093528
N-acetyl-L-ornithine	2.0865	0.09428
D-sedoheptulose-1-7-phosphate	2.1198	0.094491
2-hydroxygluterate	1.341	0.09803
1-Methyl-Histidine	2.2236	0.098122
Arginine	2.16	0.099435
N-acetyl-glutamate	1.2353	0.10208
a-ketoglutarate	0.50315	0.10389
Uric acid	2.9272	0.1065
2-Hydroxy-2-methylbutanedioic acid	1.5237	0.11036
Tryptophan	1.7394	0.11182
Carbamoyl phosphate	1.2829	0.11261
Ribose-phosphate	2.3839	0.11382

cyclic-AMP	1.6744	0.11589
Citrulline	1.3093	0.12093
Thymidine	3.2985	0.12564
IDP	1.429	0.13037
D-erythrose-4-phosphate	1.622	0.134
Nicotinamide ribotide	2.0701	0.13728
Guanosine	2.4762	0.13784
Deoxyribose-phosphate	2.1856	0.13867
N-acetyl-glucosamine	1.9365	0.13969
Thymine	1.3747	0.13982
Phosphorylcholine	1.3342	0.14034
IMP	1.5135	0.14062
Sucrose	1.3192	0.14147
Creatinine	2.097	0.14255
5-methoxytryptophan	1.931	0.15054
Cysteine	0.57582	0.15512
1,3-diphopshateglycerate	2.1358	0.15938

GDP	3.1255	0.16703
N-acetyl-glutamine	2.32	0.16927
dGDP	1.5088	0.17014
Aspartate	1.4638	0.1736
CDP-choline	1.6787	0.18001
Histidinol	2.3376	0.18448
Cystathionine	2.0365	0.19852
3-S-methylthiopropionate	0.49377	0.20156
ADP	1.4708	0.20758
ADP-D-glucose	2.7984	0.20877
Phenyllactic acid	1.3554	0.2217
2,3-dihydroxybenzoic acid	3.2862	0.23472
Deoxyinosine	2.4958	0.2373
2,3-Diphosphoglyceric acid	2.3139	0.24036
Acetylphosphate	1.3356	0.24286
Taurodeoxycholic acid	0.097605	0.24979
Glutathione disulfide	1.7617	0.27903

Isocitrate	0.80737	0.27951
UDP-N-acetyl-glucosamine	1.7719	0.28024
CDP-ethanolamine	1.6406	0.29259
Cytosine	1.2269	0.3034
Thiamine-phosphate	1.7811	0.3153
Adenosine	1.3901	0.31701
dGMP	2.016	0.3172
Imidazoleacetic acid	1.1906	0.32314
Malate	1.2169	0.32705
Myo-inositol	1.4082	0.3321
Allantoin	1.7353	0.33514
3-methylphenylacetic acid	1.4031	0.34135
Methylmalonic acid	1.263	0.35643
Betaine	0.79692	0.35914
UDP-D-glucuronate	1.7663	0.36006
5-methyl-THF	0.86193	0.37396
Allantoate	1.1911	0.38248

Orotate	0.70617	0.38519
Homocysteic acid	0.19625	0.40877
3-phosphoglycerate	1.4651	0.41313
Nicotinate	1.4472	0.42127
Thiamine pyrophosphate	2.0587	0.43321
Hydroxyphenylpyruvate	1.3752	0.43874
Maleic acid	1.2385	0.4498
Orotidine-5-phosphate	0.6881	0.45174
sn-glycerol-3-phosphate	1.1295	0.46081
2-oxobutanoate	1.1937	0.46975
S-methyl-5-thioadenosine	1.4151	0.47069
7-methylguanosine	2.131	0.47222
Fumarate	1.2174	0.47269
Dephospho-CoA	1.741	0.47378
Indole-3-carboxylic acid	0.76051	0.47555
Glucose-1-phosphate	1.2571	0.48067
Cellobiose	1.5175	0.49047

Fructose-6-phosphate	1.2143	0.49688
Fructose-1,6-bisphosphate	1.2605	0.49777
Aminoimidazole carboxamide ribonucleotide	1.386	0.4981
2-keto-isovalerate	1.2004	0.49855
Citrate	1.1805	0.50063
Quinolinate	0.68095	0.50451
Glyoxylate	1.3111	0.51298
Homocysteine	1.3886	0.52119
Xanthurenic acid	1.1032	0.53282
Acetoacetate	0.78141	0.53521
4-Pyridoxic acid	2.36	0.54929
Ethanolamine	1.2546	0.55142
Dimethylglycine	1.2978	0.55594
CDP	0.74482	0.55689
D-glucarate	1.2742	0.56572
Adenosine 5-phosphosulfate	1.2437	0.57433
Oxaloacetate	1.1714	0.58046

Glucose-6-phosphate	1.2929	0.02612768
2-ketohaxanoic acid	1.1574	0.60956
Spermidine	1.373	0.61116
Succinate	1.1482	0.61638
UDP	0.79562	0.61947
p-hydroxybenzoate	1.4518	0.63134
Putrescine	1.3539	0.63794
dTMP	1.1579	0.6464
Citraconic acid	0.94238	0.64844
Dihydroorotate	0.49356	0.6485
Dihydroxy-acetone-phosphate	1.1075	0.65552
Sedoheptulose 1,7-bisphosphate	0.68841	0.67196
UDP-D-glucose	1.2586	0.6844
Glutathione	0.82922	0.69065
Glycolate	1.2389	0.71152
Acadesine	1.2883	0.71185
2-dehydro-D-gluconate	1.1634	0.71994

NADH	0.85133	0.72239
Anthranilate	0.87639	0.74759
Carnitine	0.91398	0.75708
Homoserine	1.3347	0.76763
ATP	1.0883	0.80223
Glucosamine	1.0992	0.81877
FAD	1.0589	0.82285
Glycine	1.2057	0.82414
Aminoadipic acid	0.93545	0.83387
Hydroxyphenylacetic acid	0.88703	0.83931
Hydroxyisocaproic acid	1.0713	0.83956
Pantothenate	0.96528	0.85228
Biotin	0.9045	0.85299
5-phosphoribosyl-1-pyrophosphate	1.074	0.86672
Shikimate-3-phosphate	1.052	0.87421
Phosphoenolpyruvate	0.91001	0.87637
D-glyceraldehdye-3-phosphate	0.92269	0.89338

dGTP	0.95098	0.8939
Cholesteryl sulfate	1.0484	0.89508
p-aminobenzoate	0.95321	0.90024
Indoleacrylic acid	1.0678	0.91378
Urea	1.0641	0.92072
2-oxo-4-methylthiobutanoate	1.0977	0.92386
3-phospho-serine	0.93739	0.92618
Phenylpyruvate	0.94663	0.94931
UMP	0.97833	0.95414
Betaine aldehyde	1.016	0.95512
Glycerate	0.97209	0.96264
dTDP	1.0321	0.96558
Riboflavin	1.0424	0.97197
Flavone	1.0062	0.98083
Deoxyguanosine	0.9965	0.99705

References

1. H. Buchwald, Y. Avidor, E. Braunwald, M. D. Jensen, W. Pories, K. Fahrbach, K. Schoelles, Bariatric surgery: A systematic review and meta-analysis. *JAMA* **292**, 1724–1737 (2004). doi:10.1001/jama.292.14.1724 Medline

2. L. Sjöström, A. K. Lindroos, M. Peltonen, J. Torgerson, C. Bouchard, B. Carlsson, S. Dahlgren, B. Larsson, K. Narbro, C. D. Sjöström, M. Sullivan, H. Wedel; Swedish Obese Subjects Study Scientific Group, Lifestyle, diabetes, and cardiovascular risk factors 10 years after bariatric surgery. *N. Engl. J. Med.* **351**, 2683–2693 (2004). doi:10.1056/NEJMoa035622 Medline

3. M. A. Stefater, H. E. Wilson-Pérez, A. P. Chambers, D. A. Sandoval, R. J. Seeley, All bariatric surgeries are not created equal: insights from mechanistic comparisons. *Endocr. Rev.* **33**, 595–622 (2012). doi:10.1210/er.2011-1044 Medline

4. G. Mingrone, S. Panunzi, A. De Gaetano, C. Guidone, A. Iaconelli, L. Leccesi, G. Nanni, A. Pomp, M. Castagneto, G. Ghirlanda, F. Rubino, Bariatric surgery versus conventional medical therapy for type 2 diabetes. *N. Engl. J. Med.* **366**, 1577–1585 (2012). doi:10.1056/NEJMoa1200111 Medline

5. P. R. Schauer, S. R. Kashyap, K. Wolski, S. A. Brethauer, J. P. Kirwan, C. E. Pothier, S. Thomas, B. Abood, S. E. Nissen, D. L. Bhatt, Bariatric surgery versus intensive medical therapy in obese patients with diabetes. *N. Engl. J. Med.* **366**, 1567–1576 (2012). doi:10.1056/NEJMoa1200225 Medline

6. L. M. Carlsson, M. Peltonen, S. Ahlin, Å. Anveden, C. Bouchard, B. Carlsson, P. Jacobson, H. Lönroth, C. Maglio, I. Näslund, C. Pirazzi, S. Romeo, K. Sjöholm, E. Sjöström, H. Wedel, P. A. Svensson, L. Sjöström, Bariatric surgery and prevention of type 2 diabetes in Swedish obese subjects. *N. Engl. J. Med.* **367**, 695–704 (2012). doi:10.1056/NEJMoa1112082 Medline

7. W. J. Pories, M. S. Swanson, K. G. MacDonald, S. B. Long, P. G. Morris, B. M. Brown, H. A. Barakat, R. A. deRamon, G. Israel, J. M. Dolezal, L. Dohm, Who would have thought it? An operation proves to be the most effective therapy for adult-onset diabetes mellitus. *Ann. Surg.* **222**, 339–352 (1995). doi:10.1097/00000658-199509000-00011 Medline

8. B. Laferrère, Do we really know why diabetes remits after gastric bypass surgery? *Endocrine* **40**, 162–167 (2011). doi:10.1007/s12020-011-9514-x Medline

9. D. E. Cummings, Metabolic surgery for type 2 diabetes. *Nat. Med.* **18**, 656–658 (2012). doi:10.1038/nm.2773 Medline

10. D. Bradley, C. Conte, B. Mittendorfer, J. C. Eagon, J. E. Varela, E. Fabbrini, A. Gastaldelli, K. T. Chambers, X. Su, A. Okunade, B. W. Patterson, S. Klein, Gastric bypass and banding equally improve insulin sensitivity and β cell function. *J. Clin. Invest.* **122**, 4667–4674 (2012). doi:10.1172/JCI64895 Medline

11. A. T. Stearns, A. Balakrishnan, A. Tavakkolizadeh, Impact of Roux-en-Y gastric bypass surgery on rat intestinal glucose transport. *Am. J. Physiol. Gastrointest. Liver Physiol.* **297**, G950–G957 (2009). doi:10.1152/ajpgi.00253.2009 Medline

12. M. B. Mumphrey, L. M. Patterson, H. Zheng, H. R. Berthoud, Roux-en-Y gastric bypass surgery increases number but not density of CCK-, GLP-1-, 5-HT-, and neurotensin-

expressing enteroendocrine cells in rats. *Neurogastroenterol. Motil.* **25**, e70–e79 (2013). doi:10.1111/nmo.12034 Medline

13. E. Spak, P. Björklund, H. F. Helander, M. Vieth, T. Olbers, A. Casselbrant, H. Lönroth, L. Fändriks, Changes in the mucosa of the Roux-limb after gastric bypass surgery. *Histopathology* **57**, 680–688 (2010). doi:10.1111/j.1365-2559.2010.03677.x Medline
14. E. Taqi, L. E. Wallace, E. de Heuvel, P. K. Chelikani, H. Zheng, H. R. Berthoud, J. J. Holst, D. L. Sigalet, The influence of nutrients, biliary-pancreatic secretions, and systemic trophic hormones on intestinal adaptation in a Roux-en-Y bypass model. *J. Pediatr. Surg.* **45**, 987–995 (2010). doi:10.1016/j.jpedsurg.2010.02.036 Medline
15. C. W. le Roux, C. Borg, K. Wallis, R. P. Vincent, M. Bueter, R. Goodlad, M. A. Ghatei, A. Patel, S. R. Bloom, S. J. Aylwin, Gut hypertrophy after gastric bypass is associated with increased glucagon-like peptide 2 and intestinal crypt cell proliferation. *Ann. Surg.* **252**, 50–56 (2010). doi:10.1097/SLA.0b013e3181d3d21f Medline
16. M. Bueter, C. Löwenstein, T. Olbers, M. Wang, N. L. Cluny, S. R. Bloom, K. A. Sharkey, T. A. Lutz, C. W. le Roux, Gastric bypass increases energy expenditure in rats. *Gastroenterology* **138**, 1845–1853, 1853.e1 (2010). doi:10.1053/j.gastro.2009.11.012 Medline
17. J. Kucharczyk, E. Nestoridi, S. Kvas, R. Andrews, N. Stylopoulos, Probing the mechanisms of the metabolic effects of weight loss surgery in humans using a novel mouse model system. *J. Surg. Res.* **179**, e91–e98 (2013). doi:10.1016/j.jss.2012.02.036 Medline
18. E. Nestoridi, S. Kvas, J. Kucharczyk, N. Stylopoulos, Resting energy expenditure and energetic cost of feeding are augmented after Roux-en-Y gastric bypass in obese mice. *Endocrinology* **153**, 2234–2244 (2012). doi:10.1210/en.2011-2041 Medline
19. Materials and methods are available as supplementary materials on *Science* Online.
20. S. Y. Lunt, M. G. Vander Heiden, Aerobic glycolysis: meeting the metabolic requirements of cell proliferation. *Annu. Rev. Cell Dev. Biol.* **27**, 441–464 (2011). doi:10.1146/annurev-cellbio-092910-154237 Medline
21. M. G. Vander Heiden, L. C. Cantley, C. B. Thompson, Understanding the Warburg effect: The metabolic requirements of cell proliferation. *Science* **324**, 1029–1033 (2009). doi:10.1126/science.1160809 Medline
22. B. Thorens, Glucose transporters in the regulation of intestinal, renal, and liver glucose fluxes. *Am. J. Physiol.* **270**, G541–G553 (1996). Medline
23. J. Pácha, Development of intestinal transport function in mammals. *Physiol. Rev.* **80**, 1633–1667 (2000). Medline
24. Y. Falkén, P. M. Hellström, J. J. Holst, E. Näslund, Changes in glucose homeostasis after Roux-en-Y gastric bypass surgery for obesity at day three, two months, and one year after surgery: role of gut peptides. *J. Clin. Endocrinol. Metab.* **96**, 2227–2235 (2011). doi:10.1210/jc.2010-2876 Medline
25. J. M. Isbell, R. A. Tamboli, E. N. Hansen, J. Saliba, J. P. Dunn, S. E. Phillips, P. A. Marks-Shulman, N. N. Abumrad, The importance of caloric restriction in the early improvements in insulin sensitivity after Roux-en-Y gastric bypass surgery. *Diabetes Care* **33**, 1438–1442 (2010). doi:10.2337/dc09-2107 Medline

26. H. E. Wilson-Pérez, A. P. Chambers, K. K. Ryan, B. Li, D. A. Sandoval, D. Stoffers, D. J. Drucker, D. Pérez-Tilve, R. J. Seeley, Vertical sleeve gastrectomy is effective in two genetic mouse models of glucagon-like Peptide 1 receptor deficiency. *Diabetes* **62**, 2380–2385 (2013). doi:10.2337/db12-1498 Medline

27. S. Troy, M. Soty, L. Ribeiro, L. Laval, S. Migrenne, X. Fioramonti, B. Pillot, V. Fauveau, R. Aubert, B. Viollet, M. Foretz, J. Leclerc, A. Duchampt, C. Zitoun, B. Thorens, C. Magnan, G. Mithieux, F. Andreelli, Intestinal gluconeogenesis is a key factor for early metabolic changes after gastric bypass but not after gastric lap-band in mice. *Cell Metab.* **8**, 201–211 (2008). doi:10.1016/j.cmet.2008.08.008 Medline

28. B. S. Wolff, K. Meirelles, Q. Meng, M. Pan, R. N. Cooney, Roux-en-Y gastric bypass alters small intestine glutamine transport in the obese Zucker rat. *Am. J. Physiol. Gastrointest. Liver Physiol.* **297**, G594–G601 (2009). doi:10.1152/ajpgi.00104.2009 Medline

29. M. T. Hayes, J. Foo, V. Besic, Y. Tychinskaya, R. S. Stubbs, Is intestinal gluconeogenesis a key factor in the early changes in glucose homeostasis following gastric bypass? *Obes. Surg.* **21**, 759–762 (2011). doi:10.1007/s11695-011-0380-7 Medline

30. F. Rubino, A. Forgione, D. E. Cummings, M. Vix, D. Gnuli, G. Mingrone, M. Castagneto, J. Marescaux, The mechanism of diabetes control after gastrointestinal bypass surgery reveals a role of the proximal small intestine in the pathophysiology of type 2 diabetes. *Ann. Surg.* **244**, 741–749 (2006). doi:10.1097/01.sla.0000224726.61448.1b Medline

31. F. Rodieux, V. Giusti, D. A. D'Alessio, M. Suter, L. Tappy, Effects of gastric bypass and gastric banding on glucose kinetics and gut hormone release. *Obesity (Silver Spring)* **16**, 298–305 (2008). doi:10.1038/oby.2007.83 Medline

32. G. Wang, K. Agenor, J. Pizot, D. P. Kotler, Y. Harel, B. J. Van Der Schueren, I. Quercia, J. McGinty, B. Laferrère, Accelerated gastric emptying but no carbohydrate malabsorption 1 year after gastric bypass surgery (GBP). *Obes. Surg.* **22**, 1263–1267 (2012). doi:10.1007/s11695-012-0656-6 Medline

33. M. Yuan, S. B. Breitkopf, X. Yang, J. M. Asara, A positive/negative ion-switching, targeted mass spectrometry-based metabolomics platform for bodily fluids, cells, and fresh and fixed tissue. *Nat. Protoc.* **7**, 872–881 (2012). doi:10.1038/nprot.2012.024 Medline

34. J. Xia, D. S. Wishart, Web-based inference of biological patterns, functions and pathways from metabolomic data using MetaboAnalyst. *Nat. Protoc.* **6**, 743–760 (2011). doi:10.1038/nprot.2011.319 Medline

35. J. Vandesompele, K. De Preter, F. Pattyn, B. Poppe, N. Van Roy, A. De Paepe, F. Speleman, Accurate normalization of real-time quantitative RT-PCR data by geometric averaging of multiple internal control genes. *Genome Biol.* **3**, research0034 (2002). doi:10.1186/gb-2002-3-7-research0034 Medline

36. L. C. Aiello, P. Wheeler, The expensive tissue hypothesis: the brain and the digestive system in human and primate evolution. *Curr. Anthropol.* **36**, 199 (1995). doi:10.1086/204350

37. J. P. Wilson, Surface area of the small intestine in man. *Gut* **8**, 618–621 (1967). doi:10.1136/gut.8.6.618 Medline